Surface deformation during the 1928 fissure eruption of Mt Etna (Italy): insights from field data and FEM numerical modelling

Alessandro Tibaldi [1,2], Fabio L. Bonali [1,2], Noemi Corti [1], Elena Russo [1,2], Kyriaki Drymoni[1], Emanuela De Beni [3], Stefano Branca [3], Marco Neri [3], Massimo Cantarero [3], Federico Pasquarè Mariotto [4]

[1] Department of Earth and Environmental Sciences, University of Milan-Bicocca, 20126 Milan, Italy
[2] CRUST-Interuniversity Center for 3D Seismotectonics with Territorial Applications, 66100 Chieti Scalo, Italy
[3] National Institute of Geophysics and Volcanology, Section of Catania, Italy
[4] Department of Human and Innovation Sciences, Insubria University, Como, Italy

Abstract

The 1928 AD volcanic activity on eastern Etna, Italy, produced wide surface deformation and high effusion rates along fissures, with excess volumes of about 50 million m^3 of lavas. This, in conjunction with the low elevation of the main eruptive vents (1150 m a.s.l.), caused the destruction of the Mascali town. Our research focuses on a multidisciplinary study from field observations and Finite Element Method modelling through COMSOL Multiphysics®, with the aim of reconstructing the geometry, kinematics and origin of the system of faults and fissures formed during the 1928 event. We collected quantitative measurements from 438 sites of azimuth values, opening direction and aperture amount of dry fissures, and attitude and vertical offsets of faults. From west to east, four volcanotectonic settings have been identified, related to dike propagation in the same direction: 1) a sequence of 8 eruptive vents, surrounded by a 385-m wide graben, 2) a 2.5-km long single eruptive fissure, 3) a half-graben as wide as 74 m and a symmetric, 39-m-wide graben without evidence of eruption, 4) alignment of lower vents along the pre-existing Ripe della Naca faults. Field data, along with historical aerial photos, became inputs to FEM numerical models. The latter allowed us to investigate the connection between diking and surface deformation during the 1928 event, subject to a range of overpressure values (1-20 MPa), host rock properties (1-30 GPa) and geometrical complexity (stratigraphic sequence, layer thickness). In addition, we

studied the distribution of tensile and shear stresses above the dike tip and gained insights into dike-induced graben scenarios. Our multidisciplinary study reports that soft (e.g. tuff) layers can act as temporary stress barriers and control the surface deformation scenarios (dike-induced graben, single fracture or eruptive fissures) above a propagating dike by suppressing the distribution of shear stresses towards the surface.

Keywords: 1928 Mt Etna eruption, graben, dike, fissures, numerical modelling

1. Introduction

Magma ascent in the shallow crust occurs in the form of vertical to subvertical tabular bodies, i.e. dikes or inclined sheets (Bates and Jackson, 1987; Ferrari et al., 1991; Acocella and Neri, 2009; Acocella et al., 2009; Geshi and Neri, 2014; Falsaperla and Neri, 2015; Tibaldi, 2015; Acocella 2021). Dikes/sheets rupture the host rock ahead of their tips and form Mode I fractures (Anderson, 1951; Rubin and Pollard, 1987) driven mainly by the internal magma overpressure towards the surface (Gudmundsson, 2011). The dike/sheet ascending path generally lies on a plane parallel to the maximum principal compressive stress (σ_1) and perpendicular to the minimum principal compressive stress (σ_3) (Anderson, 1951; Rubin, 1998) ahead of the dike tip. However, subject to stress rotations, magma can stall and store along horizontal to sub-horizontal planes, forming sills (Pollard and Johnson, 1973; Maccaferri et al., 2011; Craig et al., 2016; Sili et al., 2019). Sills can then evolve to shallow magma chambers (Barnett and Gudmundsson, 2014; Gudmundsson, 2020), or can deviate along pre-existing fractures (faults or dikes) (Bahat, 1980; Gautneb et al., 1989; Ferrari et al., 1991; Garduño et al., 1996; Gudmundsson et al., 2001; Acocella et al., 2006a; Neri et al., 2008, 2011; Tibaldi et al., 2008; Ruch et al., 2016; Gudmundsson, 2020; Acocella, 2021; Thiele et al., 2021; Drymoni et al., 2021).

Fracture formation relies on the Griffith's theory, where several minor pre-existing cracks in an interface can unify to form larger cracks and eventually fractures (Griffith, 1924; Broek, 1982; Gudmundsson, 2011). In magma-driven fractures,

magma overpressure induces stress concentration at the dike tip that, in turn, can initiate and allow a fracture to propagate if: 1) the tensile stress is equal (or exceeds) the tensile strength (T_o) of the host rock, and 2) the elastic energy release rate (G_I) is equal (or exceeds) the material toughness (G_{IC}) of the host rock. If both conditions are satisfied, a fracture initiates and then propagates in advance of the magma front. Sometimes a dry segment may form at the surface (Warpinski, 1985; Bonafede and Olivieri, 1995; Garagash and Detournay, 2000; Billi et al., 2003; Tibaldi, 2015). Similarly, for a shear fracture, uniform shear (Mode II) loading conditions can also generate slip on the crack surface and promote displacement orthogonal to the crack front but parallel to the crack plane. In this case, crack generation occurs when the stress intensity factor (K_{II}), or fracture toughness of the host rock, becomes critical (K_{IIC}) (Backers and Stephansson, 2012).

In shallow settings, the stress concentration (tensile loading) above the propagating dike tip induces tensile stress (σ) and shear stress (τ) concentration in the conterminous host rock (Gudmundsson, 2011). As a result, at a short distance from the tip's side there is a great concentration of tensile stress which is thus subject to shear stress. This may produce deformation of the topographic surface and can be expressed by the formation and development of extension fractures, faulting, upwarping, and graben development (Rubin and Pollard, 1988; Billi et al., 2003). The dike-induced surface deformations can be further convoluted owing to the different geometries of the intrusion plane, the dissimilar mechanical layering of the host rock, and topographic effects (e.g.: Acocella et al., 2006b, 2009; Neri et al., 2008; Bonforte et al., 2009; Battaglia et al., 2011; Trippanera et al., 2014, 2015; Galland et al., 2015; Guldstrand et al., 2017; Fittipaldi et al., 2019; Gudmundsson, 2020; Tibaldi et al., 2020; Drymoni et al., 2021). Although these topics have already been studied, more field observations and analyses are needed to better understand the complex relationships between them.

With this paper, we intend to contribute to a better understanding of dike-induced surface deformations in central stratovolcanoes, taking as a field-based example the structures associated with the eruptive fissuring of 1928 AD at Mt Etna, Italy (Duncan et al., 1996; Branca et al., 2017). This volcano is subject to both tectonic, magmatic

and gravity stresses, which interact triggering eruptions. The eruption here studied started in November 1928 with the opening of three eruptive fissures (UF, MF, LF in Fig. 1), aligned in a WSW-ENE direction. These three fissures opened in time progression on the 2nd, 3rd, and 4th-19th November, and thus propagated eastward (Branca et al., 2017), coherently with the presence of a dike that intruded in the same direction. They started in the summit area of the volcano, but quickly, in a few days, propagated down to 1150 m a.s.l. (Duncan et al., 1996; Branca et al., 2017). From this site, a long lava flow expanded downward and covered an area of 4.38 km^2, destroying the village of Mascali and sterilising wide swaths of productive agricultural land.

The structures associated with the 1928 fissure eruption of Mt Etna provide an excellent case study, because they show a plethora of possible dike-induced structures, such as symmetric to half-grabens, dry fissures, volcanic vents and eruptive fissures. The integration of field observations with aerial remote-sensing analysis allowed us to precisely map and quantify the structures: these data, together with lithostratigraphic observations, became inputs to FEM models to investigate the scenarios that lead to the observed dike-induced surface features. Further sensitivity analysis allowed us to investigate the parameters that control the surface deformation subject to a range of overpressure values (1-20 MPa), host rock properties (1-30 GPa) and geometrical complexity (stratigraphic sequence, layer thickness). The results of our study have a wide impact and interest as they provide a crucial contribution to the understanding of dike-induced deformation in active volcanic areas and could be broadly applied in similar volcanotectonic settings elsewhere.

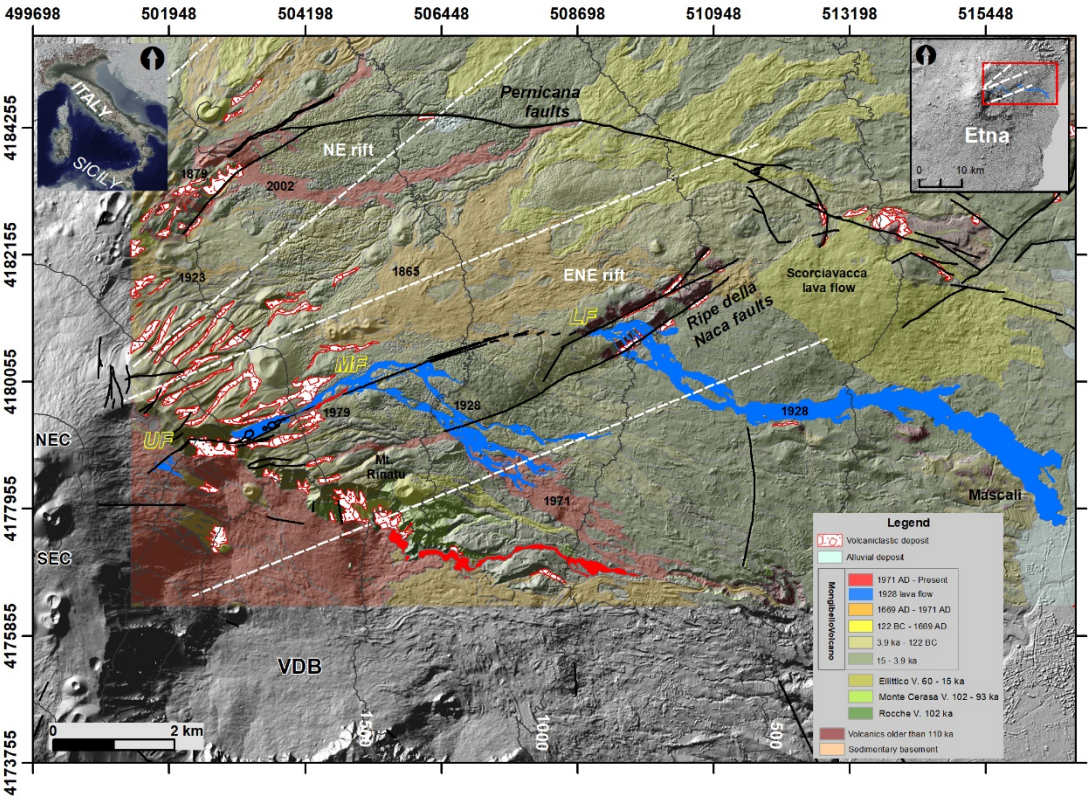

Figure 1. *Geological map of the studied area overlapped on a shaded relief (http://geodb.ct.ingv.it/geoportale/; Branca et al., 2011). The two insets show the location of Mt Etna and the studied area. The white dashed lines delimit the NE Rift and the ENE Rift. The numbers specify the age of flank eruptions. Black lines indicate the main faults (after Azzaro et al., 2012). UF= Upper Fracture, MF=Middle Fracture, and LF = Lower Fracture are the segments of the 1928 fracture swarm. Contour lines every 500 m were extracted from the 2005 DEM by Gwinner at al. (2006). VDB = Valle Del Bove, SEC = SouthEast Crater, NEC = NorthEast Crater.*

2. Geological background

Mt Etna is a large basaltic composite stratovolcano formed during the last 500 ka in eastern Sicily. Its geological evolution is divided in four main evolutionary phases of eruptive activity: the Basal Tholeiitic (500-330 ka), Timpe (220-110 ka), Valle del Bove (110-60 ka) and Stratovolcano (60 ka-Present) phases (Branca et al., 2011a, b). The eastern flank of the volcano is distinguished by the presence of a wide

depression with an amphitheater shape, known as Valle del Bove; our study area is located immediately NE of the northern escarpment of the Valle del Bove, which is formed by volcanic deposits of the Valle del Bove phase related to the eruptive activity of Rocche and Mt Cerasa volcanoes (Fig. 1). These deposits are covered by the thick succession of Ellittico volcano, consisting of alternating lava flows and pyroclastic deposits emplaced between about 60 and 15 ka ago. Eruptive activity in the last 15 ka, belonging to Mongibello volcano, covered the main portion of the investigated area generating the present morphological setting of the Etna edifice. The Mongibello volcanic succession mainly consists of lava flows, generated by both summit and flank eruptions, and subsequently by pyroclastic fall deposits (Branca et al., 2011a, b).

The eruptive fissures of Mongibello volcano are spatially clustered according to two main weakness zones, named North-East Rift and ENE Rift (Fig. 1) (Kieffer, 1975, 1985; Lo Giudice et al., 1982; McGuire and Pullen, 1989; Patanè et al., 2011; Cappello et al., 2012; Azzaro et al., 2012), which represent ideal locations for magma rising, giving place to flank (or lateral) eruptions, that are usually fed by shallow (1–3 km in depth) dikes propagating laterally from the central conduit (Acocella and Neri, 2009). The North-East Rift, located on the upper northeastern flank of the volcano, is represented by a swarm of eruptive and dry fissures striking in NNE- to NE direction, pit craters and pyroclastic cones, 0.5 km wide and about 7 km long, which stretches from 2500 to 1700 m a.s.l. More in detail, eruptive fissures strike from N15°E to N50°E, showing a gradual clockwise rotation along the rift towards NE (Tibaldi and Groppelli, 2002). Along the northern shoulder of the Valle del Bove, the ENE Rift is composed of another smaller swarm of dry and eruptive fissures and cones, at about 2300-1600 m a.s.l. of elevation; fissures strike from N70°E to N90°E (Azzaro et al., 2012). The eruptive fissures of the ENE Rift formed during flank eruptions that took place between 15 ka and 3.9 ka BP (Branca et al., 2011a): some of these fissures propagated from the northern escarpment of the Valle del Bove down to the fault scarps of the Ripe della Naca (Fig. 1). In historical times, during the past 2500 years, several eruptive fissures intruded along the ENE Rift and they are related to the eruptions of Mt Rinatu, dated 1000 ± 50 AD, and Scorciavacca,

dated 1020 ± 40, 1865, 1928, 1971 and 1979 AD (Branca et al., 2011a). The topic of our study, which is the 1928 fissure eruption, is characterised by a swarm of fractures and eruptive vents extending from the northern bottom of the Valle del Bove to the west, to the intersection with the Ripe della Naca faults to the east (Figs. 1 and 4F).

The 1928 eruption is the only event, following that of 1669, to have caused the destruction of a town in the Etna region. This eruption involved the north-eastern flank, and the opening of the fissure system, which started on November 2nd, and was preceded and accompanied by intense explosive activity at the NE crater (Branca et al., 2017). On that day, the first segment of the fissure formed at 2600 m a.s.l. and extended for 450 m, with activity lasting less than 1 hour that produced a short, 0.45 km-long lava flow. The second segment of the fissure opened on November 3rd more to the east, at Serra delle Concazze, between 2300 m and 1560 m a.s.l., extending for 3.2 km. This fissure emitted a lava flow for about 18 hours, that destroyed conterminous woods, reaching 3.8 km in length. The third segment of the fissure, 100 m-long, formed further east during the night of November 4th at 1200 m a.s.l. at Ripe della Naca. The development of this dry and eruptive fracture swarm from west to east clearly mirrors a propagation in the same direction of the feeder dike. A lava flow was issued from the third fissure and advanced rapidly (0.46 km/h) along the Pietrafucile-Vallonazzo stream gully, reaching, on the morning of November 6th, the town of Mascali, which was destroyed the following day, with the exception of the small neighborhood of Sant'Antonino. Between November 6th and 10th, the advance of the lava flow interrupted all communication routes between the cities of Catania and Messina, resulting in about 5000 homeless people and causing the destruction of 716 hectares of productive land and 8 industrial plants for the processing of citrus fruits. During the night of November 19th, the emission of lava ended, generating overall a flow 9.4 km in length that reached an elevation of 25 m a.s.l. and destroyed a few houses in the village of Carrabba. After 17 days of activity, a total lava volume of 52.9 ± 5.2 × 106 m^3 had been erupted, with an average effusion rate of 38.5 m^3/s (Branca et al., 2017).

3. Methodology

3.1 Field and historical aerial photo analysis

In order to map and classify all the structures of the area in detail, we carried out a remote-sensing analysis by means of historical aerial photos. We used aerial photos collected in 1932, 1954 and 1955 by the Istituto Geografico Militare (I.G.M., https://www.igmi.org/). Their comparison allowed us to distinguish the 1928 associated structures with the ones generated by later eruptive activity in the same area (1971 and 1979 AD).

Then, we performed a detailed field survey along the entire length (14 km) of the 1928 fissure, by collecting quantitative and qualitative structural measurements, and to validate the classification made through the remote sensing analysis. We classified the observed fractures as normal faults when they presented a vertical offset (Fig. 2A), or as extension fractures when there is no vertical displacement (Fig. 2B). In some cases, sediments covered the fractures, not allowing the observation of a continuous scarp; in this case, the classification was made considering the change in the topography, when it showed a vertical offset. The surface fractures were classified either as dry fractures when they did not present eruption signs, or as eruptive fissures (Fig. 2C) when they were accompanied by spatter lavas, lava flows or scoriae deposits.

In view of the above, we performed field surveys to collect structural data at 438 sites along the 1928 fracture; each measurement was referred to the WGS84 datum using RTK GPS with 2-cm of accuracy. We made precise measurements of the strike, opening direction and aperture amount of dry fractures, and collected data regarding the attitude and offset of the mapped normal faults. To measure the vertical offset in the field, we used a measuring tape for offsets < 2 m, and a laser rangefinder for offsets > 2 m, obtaining results with an uncertainty of 0.10 m and 0.20 m, respectively. The opening direction was measured only when piercing points were clearly visible on both sides of the fracture.

We paid special attention to distinguish among structures formed during the 1928 event and those produced by earlier events. First of all, we examined the

stratigraphic relationships between the various structures and the 1928 depositional units, ascribing to pre-1928 events the structures that are clearly covered by the 1928 lava flows. Although we recognize that some uncertainty here can be present, because some faults or fissures can have formed as the dike propagated upwards or laterally prior to erupting, we used this stratigraphic criteria in conjuction to further observations. The 1928 fractures are all characterised by a very low degree of sediment infilling and young vegetation, whereas the pre-1928 structures are filled and have large trees. We also examined the fault scarps to see if there are indications of reactivation (such as different degrees of erosion of parts of the fault scarp, or different lichen colonization), without finding any evidence. Finally, there are some historical papers that describe that during the 1928 event the new swarm of fractures formed (Friedlander, 1929; Ponte, 1928, 1929; Imbò, 1932).

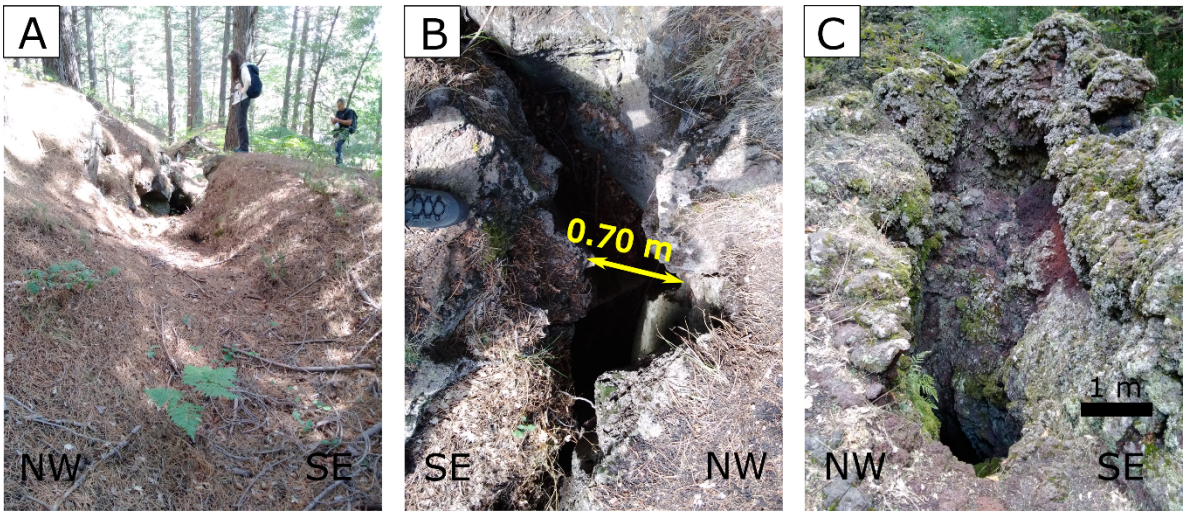

Figure 2. *View of a SE-dipping normal fault (A), a dry extension fracture (B) and an eruptive fissure with signs of spatter lava deposits (C) as surveyed in the field.*

3.2 Numerical modelling

3.2.1 Material properties

In the present research, we use a layered domain that corresponds to dissimilar Young's modulus (E) values since the upper crust is mainly highly anisotropic and heterogeneous (Gudmundsson, 2011, 2020; Drymoni et al., 2020). In detail, stiffness properties reflect values that have been proposed as common crustal deposit values

(Gudmundsson, 2011). Basement values are between 10-40 GPa, shallow crust deposits typically range between 1-15 GPa (Ray et al., 2006; Becerril et al., 2013), while pyroclastics and sediments may be very compliant, as much as 0.001 GPa (Heap et al., 2019). Furthermore, we assume that the examined crustal segment (and its associated layers) is characterised by a linear elastic behaviour, based on previous studies (e.g. Gudmundsson, 2011).

Consistently with field lithostratigraphic observations, here we consider a heterogeneous host rock, made up of an approximation of four layers, with the following characteristics: i) comparatively stiff lava flows with $E_{CS,\ CS2}$=7-10 GPa, ii) stiff host rock lava flows with E_S=7-30 GPa, and iii) a compliant tuff layer with E_T=1 GPa. All deposits have a constant Poisson's ratio value of 0.25 (Babiker and Gudmundsson, 2004) and density values of $\rho_{CS}=\rho_S$=2600 kg m^{-3} that correspond to stiff lava deposits, and ρ_T=2000 kg m^{-3} for compliant deposits.

3.2.2 FEM Methods

We used the Structural Mechanics module of the Finite-Element-Method (FEM) software COMSOL Multiphysics (v5.6), to explore the distribution of dike-induced local tensile stresses while the fracture propagates to the surface through a layered elastic medium. The program has the ability to analyse in 2D the stresses and strains at a dike tip subject to user-defined boundary conditions (dynamic boundary loads) and simulate the distribution of stresses around the tip to enable assessing both the modes of fracturing (Broek, 1982; Gudmundsson, 2011) as well as the likelihood of the dike propagation path (Drymoni et al., 2020). According to Amadei and Stephansson (1997), the tensile stress should be almost equal to the in-situ tensile strength (T_o) of the host rock for a fracture to occur (between 0.5-9 MPa); hence, in all our models we design primarly a tensile stress surface. Secondly, we explore the possibility of pre-existing fractures to slip; hence, we model also a shear stress surface (Melin, 1986; Lawn, 1993). The shear stress concentration has been proposed to be usually two times the tensile stress ($\tau \geq 2\sigma$), thus between 1-12 MPa (Haimson and Rummel, 1982; Schultz, 1995) to generate slip in pre-existing fractures. In the static models, we change the depth of the dike to allow it to

propagate gradually to the surface. While it ascends, we take snapshots of the latter on dissimilar stratigraphic contacts where a mechanical contrast can be produced (Gudmundsson and Brenner, 2001). The models assume that pre-existing fractures exist in the near-surface domain generating individually either Mode I or II fracturing scenarios (Backers and Stephansson, 2012) and that the host rock behaves in a linear elastic way (Farmer, 1983; Bell, 2000).

3.2.3 Model setups and baseline models

We designed 2D models of a dike propagating through a layered host rock subject to the following steps. First we designed the geometry of the squared layered host rock domain, which replicated the field observations, and then that of the dike (Fig. 3). The latter has been modelled as an elliptical cavity with internal overpressure of P_o=1-20 MPa for a basaltic dike, as defined by Becerril et al. (2013). We then assigned material properties (stiffness, Poisson's ratio, density) to each deposit as described above. Before running the models, we discretised the computational domain by using very fine triangular meshing, characterized by a minimum element quality of 0.4534 m and 1100 boundary triangular elements. All models are fastened in the two bottom corners to avoid rigid-body rotation and translation. Finally, the upper surface, which is considered to be flat, is free, hence simulating Earth's surface (Fig. 3). Our models are finally moved in the centre, close to the central part of the domain, to ensure that the modelled area of interest is sufficiently far from the model edges so as not to be contaminated by edge effects.

We designed a suite of baseline models with gradual complexity to simulate as much as possible the field observations and the in situ conditions during dike emplacement. We originally started from homogeneous domains and then gradually improved the host rock geometry by adding the stratigraphic sequence typically found on Mount Etna. The latter was comprised by: 1) two comparatively stiff (E_{CS}=7-10 GPa) lava layers with a measured field thickness of 1 m and 0.2m respectively, 2) a compliant tuff (E_T=1 GPa) layer with a measured field thickness of 1 m, and 3) a stiff lava layer (E_S= 7-30 GPa) which simulates the surrounding host rock in the model setups (inset in Fig. 3).

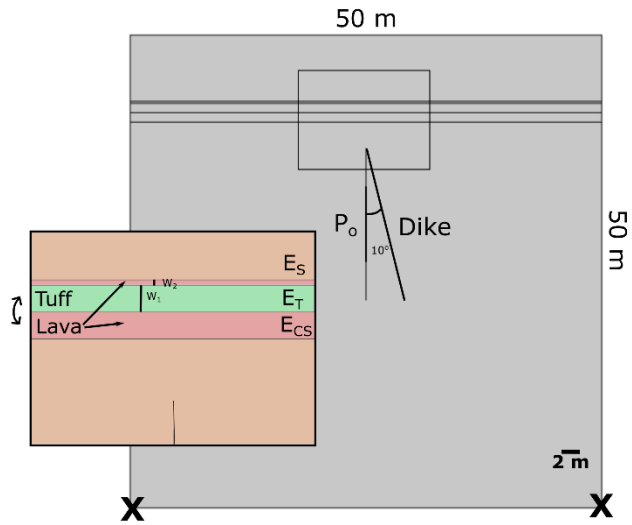

Figure 3. *Numerical model setup. The computational domain is 50 m x 50 m and the dike is located at 12 meters depth with a 0.5 m thickness, and a maximum inclination of 10°. The crosses at the two bottom corners represent fastened conditions. Host rock layering and dissimilar properties are represented by colour coding: green corresponds to tuff, red to comparatively stiff lava flows, orange to very stiff lava flows. The sensitivity analyses include changes in the sequence of the layers, the stiffness of the layers (E_{CS}, E_T, E_S), their thickness (W_1, W_2), their overpressure range (P_o=1-20 MPa) and the inclination of the propagating dike (0-10°).*

We initially plot the magnitudes (distribution) of σ_3 to examine the stress concentration around the dike tip and the location of their highest concentrations. Then, we plot a second contour (line) surface to examine similarly the shear stress concentration. Finally, we design two arrow surfaces corresponding to σ_1 and σ_3 principal compressive stresses ahead of the dike tip.

3.2.4 Sensitivity tests

We performed several sensitivity tests to investigate which are the stress conditions and the geometrical or mechanical parameters that could, individually or coupled, produce temporary stress barriers in Etna's shallow crust. For that reason, we initially

examined the effects of the dike's overpressure (P_o) in two different orders of magnitude (1 MPa and 10 MPa) within a range of 1-20 MPa, the layer thickness (W) in two different orders of magnitude (0.1 m and 1m) and within the range of 0.1-1 m. Finally we explored the stiffness (E_{CS}, E_T, E_S) of the layers in two different orders of magnitude (1 GPa and 10 GPa) and within a range of 1-30 GPa. In a second stage, we tested some further geometrical properties of the host rock, such as the stratigraphic sequence, and the dike inclination (0-10°). The detailed analysis, results and interpretations are to be presented in a numerically-focused follow up study, due to the length of the current work. Here, we provide some initial insights which could better interpret the field observations, which are the main focus of this case-study.

4. Results

4.1 Surface deformation

In the field, we recognized all the fractures and eruptive vents present along the 1928 fissure, for a total of 159, classified as: I) 11 eruptive vents formed during 1928 (7% of structures), II) 8 pre-1928 eruptive vents (5%), III) 33 eruptive fissures (21%), IV) 29 normal faults (18%), V) 38 dry extension fractures associated with the 1928 event (24%), VI) 36 older fractures (faults and extension fractures) (23%), and VII) 4 pit craters (2%), as can be seen in Fig. 4F. Furthermore, we collected structural measurements in 438 sites (Fig. 4G), as explained in the previous chapter, and we collected the strike of all fractures: the predominant direction is ENE-WSW, with the majority striking N60-70°E (Fig. 4A) (Table 1).

Table 1: Collected strike data and statistical analysis (N=136).

Classified trend	Peak strike	Average strike	Standard deviation
III) eruptive fissures	N60-70°E	N65.8°E	7.1°
IV) normal faults	N60-70°E	N72.7°E	10.1°
V) dry fractures	N70-80°E	N70.6°E	6.3°

VI) older structures	N60-70°E	N67.6°E	8.4°
Total	N60-70°E	N69.1°E	8.3°

Our observations have revealed four settings of surface deformation (Fig. 4F) along the studied profile, from west to east. In detail, we report:

1) *Sector one (Fig. 5):* A sequence of 8 eruptive vents, with an ENE-WSW alignment, surrounded by a 385-m wide graben with offset values ranging up to 10 m, an average offset of 1.8 m and a standard deviation (SD) of 2.1 m.
2) *Sector two (Fig. 6):* A single eruptive fissure, no graben formation.
3) *Sector three (Figs. 7-8):* A 74-m wide half-graben with offset values up to 1.2 m, an average offset of 0.8 m and a SD of 0.7 m, followed to the east by a 39-m-wide graben with offset values ranging from 0.9 to 1.3 m, an average offset of 1 m and a SD of 0.8 m. No evidence of eruption.
4) *Sector four:* Alignment of lower vents along the pre-existing Ripe della Naca Fault.

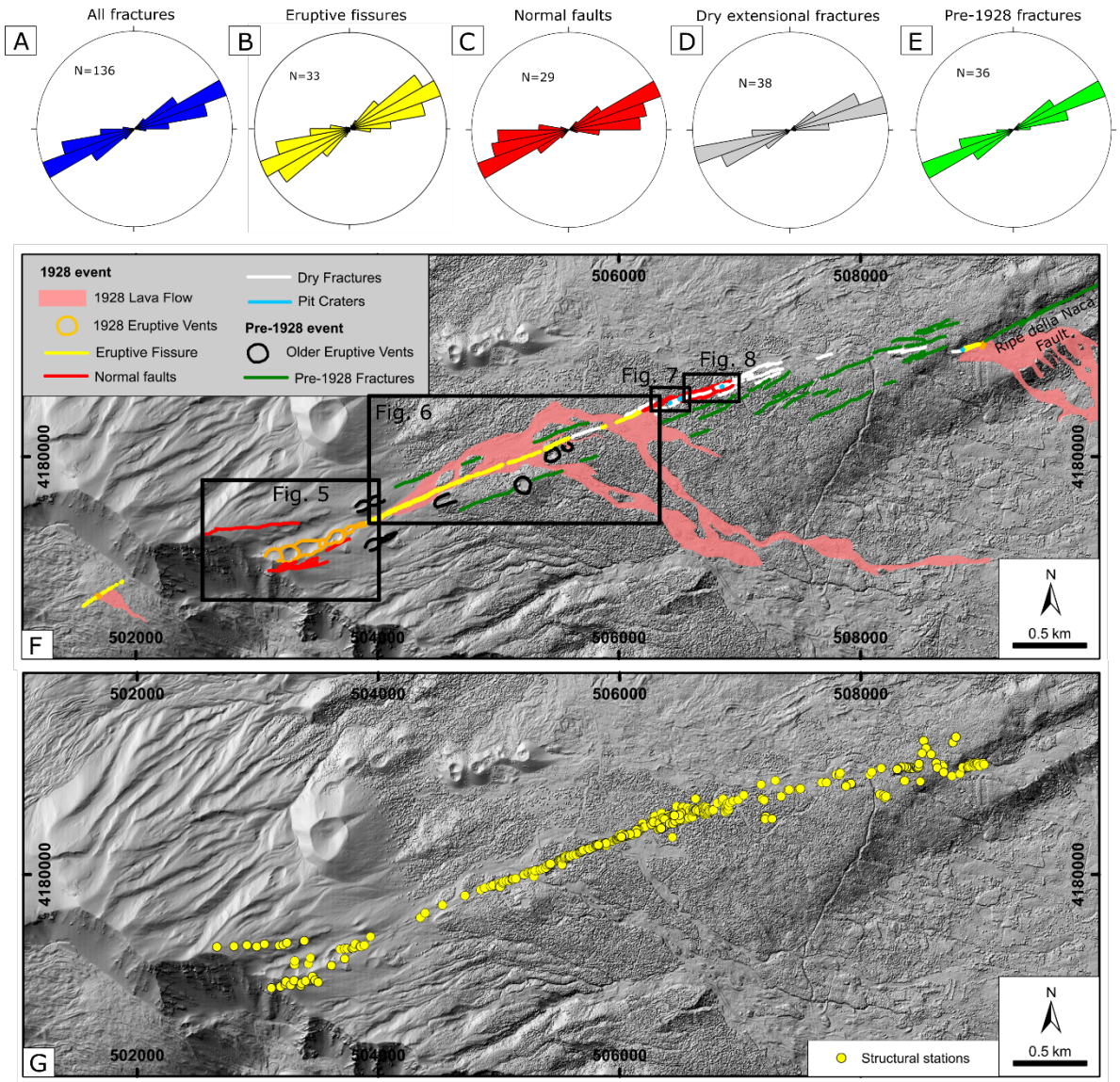

Figure 4. *Rose diagrams showing the strike of all fractures (A), eruptive fissures (B), normal faults (C), dry extension fractures (D) and older fractures (E). The structural map with the location of the different surficial deformation settings, represented more in detail in Figures 5-6-7-8, is shown in (F). The map with the location of all the sites of structural observations is shown in (G). Coordinate Reference System: WGS 84-UTM 33N.*

4.1.1 Sector 1: volcanic vents and graben

The westernmost and most elevated sector of the 1928 fissure is characterized by the alignment of 8 volcanic vents, with an average direction of crater elongation of

N67°E, in agreement with the general trend of the 1928 structure according to the statistical analysis. The vents are surrounded by normal faults with converging dips which form a 385-m wide and 10-m deep graben (Fig. 5A): faults strike E-W to ENE-WSW and multiple planes can be found along the southern side of the graben, with vertical normal offsets up to 10 m. However, the fault scarps are partially covered by younger volcanic deposits so the measured displacement is estimated. Instead, along the northern side of the graben, only one fault is present, with normal offsets ranging 1 to 3 m. The presence of all these structures in the historical aerial photos of 1932, collected by I.G.M., confirm they are linked to the 1928 event.

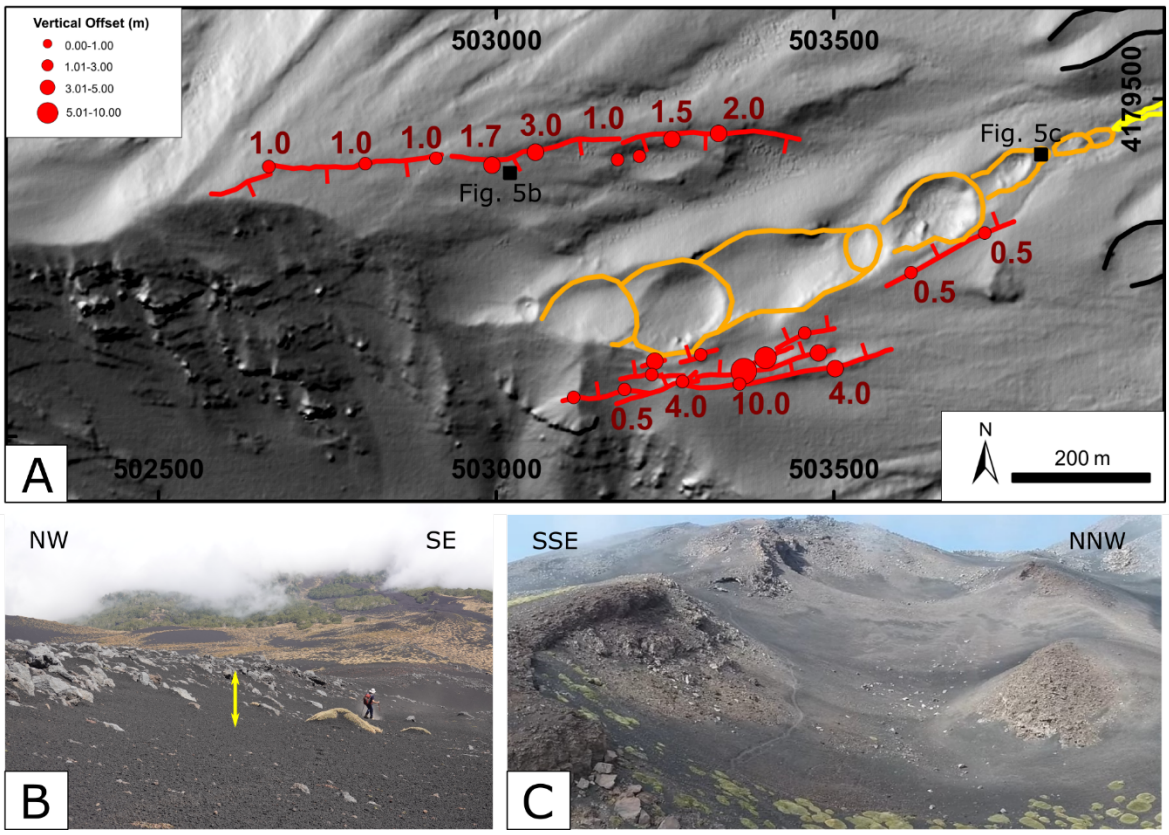

Figure 5. *(A) Map showing in detail Sector 1, where volcanic vents and the presence of a graben can be observed. Legend of the structures and location of this figure are in Figure 4F. Coordinate Reference System: WGS 84-UTM 33N. (B) and (C) show the S-dipping normal fault and WSW-ENE-aligned volcanic vents, respectively. The yellow arrow in (B) indicates the vertical normal offset.*

4.1.2 Sector 2: single eruptive fissure

Towards the east, at an altitude of ~2080 m a.s.l., the surface expression of the 1928 structure changes abruptly: here, volcanic vents are not visible anymore, whereas a single eruptive fissure can be clearly observed. This setting appears continuously for 2.5 km moving eastward, up to an altitude of ~1600 m a.s.l. There, the fissure suddenly disappears, and finally emerges again at the surface in correspondence of the lower vents (~1150 m a.s.l.), almost 3 km to the east. In this sector, there is no clear evidence of graben formation, apart from a few scattered short scarps with low offsets. Like in Sector 1, both north and south of the 1928 fractures, pre-1928 fractures have been recognized, that do not show a continuous vertical offset or evidence of graben formation, and, of course, have been excluded by the present analysis (green lines in Fig. 6A). Moreover, in the NE part of this sector, the uprise of the dike to the surface caused several collapses, forming a series of sinkholes, aligned and elongated as the fractures (Figs. 6B-C).

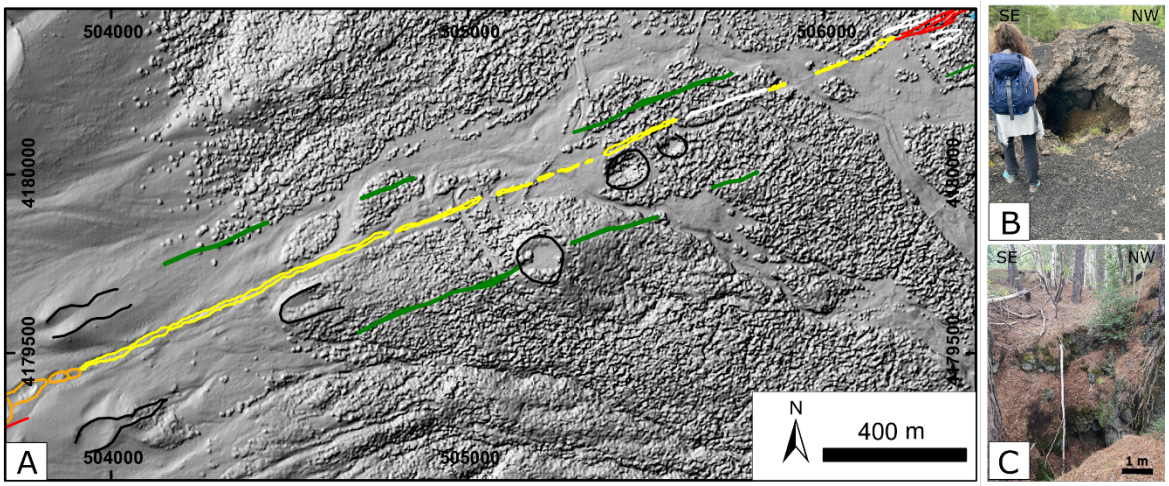

Figure 6. *(A) Map showing in detail Sector 2, where surface deformation is characterized by a single eruptive fissure without evidence of clear vertical displacement at its sides. Legend and location of this figure are in Figure 4F. Coordinate Reference System: WGS 84-UTM 33N. Examples of the eruptive fissure and a sinkhole are shown in (B) and (C).*

4.1.3 Sector 3: half-graben and symmetric graben without eruption

In this sector, located at ~1600 m a.s.l., there are no signs of eruption. The western part of the sector is characterized by the presence of a 74-m wide half-graben, as shown in detail in Figure 7A. The northern half-graben side is formed by SE-dipping normal faults (Fig. 7D), with offsets ranging from 0.3 to 1.2 m. Instead, only dry extension fractures are present along the southern side, without any evidence of vertical offset (Fig. 7E). The structural analysis of the extension fractures has shown that the maximum amount of aperture is 3 m, with an average of 1.1 m, and the standard deviation (SD) is 0.8 m. We report results from 12 sites where the opening direction has an average value of N161.2° E, and a SD of 12.4°, with a peak between N160-180°E. Considering the local strike measured in the same sites, we obtained an average of N68.9°E, and a SD of 6.3°, with a peak in the interval N60-70°E, indicating a small right-lateral component of movement of 2.3° (Fig. 7B). In detail, 6 sites show signs of pure extension (lateral component < 5°), 5 sites of right-lateral and only 1 of a left-lateral component of displacement, respectively. The opening direction values in Figure 7C are related to the local strike, since a clockwise rotation of the former corresponds also to a clockwise rotation of the latter. Finally, we report a few sinkholes in the middle part of the sector (Fig. 7A).

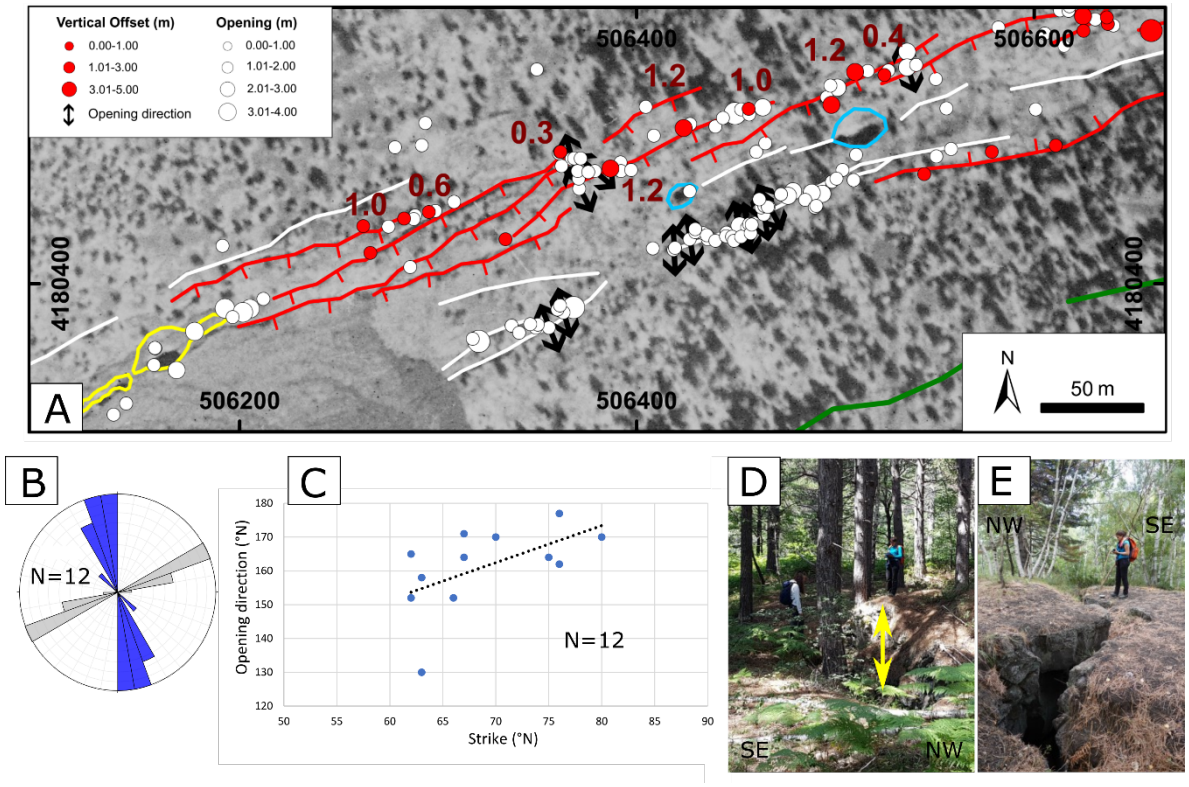

Figure 7. *(A) Map showing the western part of Sector 3. The black arrows represent the opening direction of fractures, while numbers correspond to the vertical offset (in meters) measured at the sites of structural measurements. Coordinate Reference System: WGS 84-UTM 33N. Location in Figure 4F. (B) Rose diagram showing the local strike (in grey) and the opening direction (in blue) at 12 sites, respectively. (C) Graph showing the relation between the local strike and the opening direction. (D) Field example of a SE-dipping normal fault. The yellow arrow highlights the vertical offset. (E) A dry extension fracture observed in the field.*

The eastern part of Sector 3 is characterised by a symmetric graben: the southern side is formed of NNW-dipping faults, whereas the northern side by SSE-dipping normal faults (Fig. 8A). The range of vertical offsets is between 0.3 and 3.5 m, with a maximum cumulated value of offset of 4 m along part of the northern graben side. In the middle of the graben, extension fractures were noticed, but opening directions could not be measured because piercing points were not visible. Finally, average aperture values were lower than 1 m with a maximum of 2.7 m (Fig. 8A).

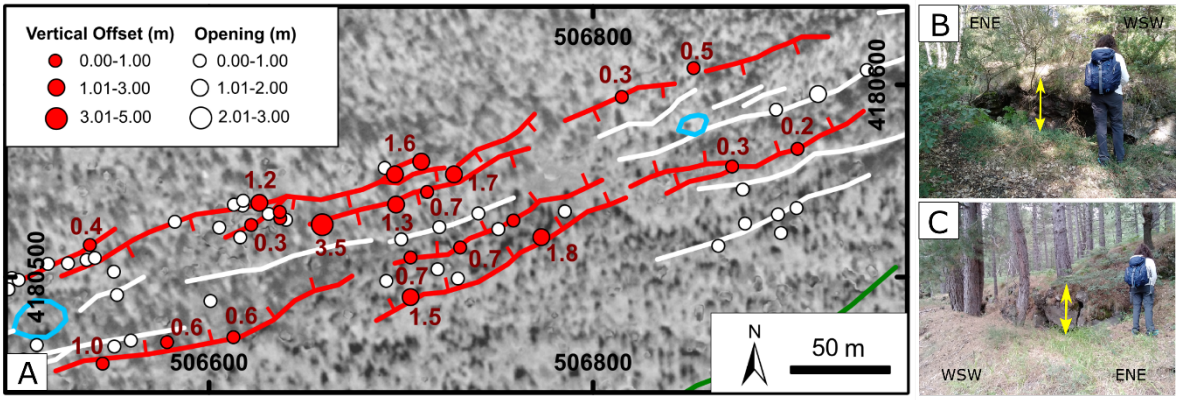

Figure 8. *(A) Map showing the eastern part of Sector 3. The numbers indicate the vertical offset (in meters) at the structural stations, while the red and white dots report the vertical offset and aperture values, respectively. Coordinate Reference System: WGS 84-UTM 33N. Location in Figure 4F. (B) A NNW-dipping and (C) a SSE-dipping normal fault are shown, along with their vertical offset, highlighted by the yellow arrow.*

4.1.4 Sector 4: lower vents and Ripe della Naca faults

This is the easternmost part of the 1928 fissure (Fig. 4), connected to Sector 3 by a number of right-stepping, dry fractures. Sector 4 is distinguished by the presence of some aligned sinkholes and a series of vents in the form of small pyroclastic cones. The craters of the cones are aligned ENE-WSW and elongated with a trend between N65°E and N74°E. These are the vents from which the long lava flow was outpoured and reached the town of Mascali, destroying it. The vents are located at the foot of the upper escarpment of the Ripe della Naca faults, in an area coinciding with the intersection between the 1928 fracture and the trace of the upper Ripe della Naca faults. Here, in fact, the Ripe della Naca faults are composed of two main normal faults striking about N70°E and dipping towards SSE. They form two escarpments: the upper one is about 90-130 m high, the lower one is about 110-125 m high.

4.2 Numerical modelling

Our main aim was to reproduce the field observations through numerical modelling and to gain insights into the connection between in depth and surface deformation processes, induced by diking. Firstly, we modelled a basaltic dike propagating towards the surface through a layered media and studied the conditions of Mode I fracturing close to the dike tip. Secondly, we explored the Mode II fracturing scenario in the vicinity of the dike tip but we also expanded our interpretations by studying the distribution of shear stress towards the surface. Finally, in both scenarios, we explored the propagation path of the dike as designated by the local stress field (σ_1 and σ_3).

In Figures 9-11, we show the results from a suite of models that simulated the observed stratigraphy. The vertical dike was modelled in a variety of setups (layering scenarios and dike inclination) with an assigned overpressure of 1 MPa (e.g. Fig. 9A), 10 MPa (e.g. Fig. 9B) and finally 20 MPa (e.g. Fig. 9C). The host rock in all models had a stiffness range of 1-30 GPa. In Figures S1-3 (Supplementary material) we report the theoretical shear stress values calculated with COMSOL multiphysics both at the very close vicinity of the dike tip and 2 m below the surface (Fig. S4 Suppl.). The model results are summarized as follows:

Figure 9 shows the results assuming a vertical dike propagating towards the surface through a layered sequence as observed in the field.The dike is modelled at the first (and deepest) soft/stiff contact (E_T/E_{CS} = 0.14), which reflects the location of the highest mechanical contrast in the layered sequence. According to the models, the tensile stresses formed by performing an overpressure boundary condition are concentrating symmetrically at the stiff lava layers and more especially at the stiffer lavas (E_S=30 GPa). In Figure 9A (P_o = 1 MPa), low to moderate tensile stress values (0.5 – 5 MPa) are concentrated in the stiff layers (lava). Also very low shear stress values (up to 2 MPa) are distributed around the dike tip, but not above it and towards the surface. The shear stress concentration at the dike tip (Figs. S1A-D Suppl.) is 0.8 to 1.4 MPa and decreases towards the surface (around 0.82 MPa at 2 m below the surface). The σ_3 trajectories at the dike tip show up to 90° rotations just above it and close to the contact between the tuff and the lava layer indicating the presence of a stress barrier. In the next model, in Figure 9B, we increased the overpressure

by one order of magnitude (P_o = 10 MPa). We observed moderate (3-5 MPa) to high (6-10 MPa) tensile stress concentration at the lava layers. At the dike tip, the σ_3 trajectories show minor rotations (up to 45°), but at the close vicinity of the tip with the comparatively stiff lava/tuff contact we observe a 90° σ_3 stress rotation, which could imply again that the tuff layer can act as a temporary stress barrier. The shearing fracturing mode distribution is also observed with the contours surface. In detail, low shear stress values (1-4 MPa) are distributed at the top lava layer, whereas the rest (5-12 MPa) are concentrated at deeper levels and mostly at the tuff (1-4 MPa) and comparatively stiff lava deposits (5-12 GPa). The theoretical shear stresses now subject to a higher overpressure show equally an order of magnitude higher values (Figs. S1B-E Suppl.) both at the dike tip (τ = 14 MPa) and close to the surface (τ = 8.2 MPa). It is clear that in Figure 9B (P_o = 10 MPa), the presence of the tuff layer suppresses the distribution of shear stresses towards the surface. Although the tensile stress is very high at the top layer, the shear stress is not sufficient to initiate slip above the dike tip and close to the surface ($\tau < 2\sigma_3$).

However, when we rise even more the dike's overpressure (P_o = 20 MPa, e.g. Fig. 9C), the tensile and shear stress distribution show another pattern. In detail, the shear stress contours are now closer to the surface and two symmetrical lobes are formed at the dike's surroundings. The top layer now bears a higher range of shearing (1-8 MPa), while the tuff layer has a range of 2-12 MPa. The theoretical shear stresses at the dike tip reach even higher values up to 28 MPa at the tip and 16.8 MPa close to the surface (Figs. S1C-F Suppl). The tensile stress is highly concentrated at the stiff lava layers and especially at the top lava layer (σ_3 = 10 MPa). A stress barrier condition still exists at the comparatively stiff lava/tuff contact above the dike tip. The comparative study of Figures 9A-C proposes that higher overpressure values result in higher tensile stress concentration at the top lava layer and eventually a higher probability of Mode I fracturing. However, our models show that the distribution of shear stress towards the surface is not only subject to the overpressure value of the dike but also to the presence of soft layers in the host rock. To identify how the stiffness of the top layer controls the concentration of tensile and shear stress regardless of the boundary conditions, we have rerun all the previous

models with a lower Young's modulus value, equal to the comparatively stiff lava (E_{CS} = E_S = 7 GPa). The results are presented in Figures 9D-F and S1G-L (Suppl.) and show that even if the top layer is softer (but still comparatively stiff), the stress concentrations are quite similar to Figures 9A-C and S1 (Suppl.). In detail, the theoretical shear stress at the tips rises from 1.4 MPa to 2 MPa for P_o=1 MPa, from 14 to 19 MPa for P_o=10 MPa and from 28 to 38 MPa for P_o=20 MPa. However, the shear stress close to the surface shows a 15% reduction from 0.82 to 0.69 MPa for P_o=1 MPa, 8.2 to 6.9 MPa for 10 MPa and finally 16.4 to 13.8 for P_o=20 MPa. This implies that Mode I and II fractures can occur very close to the tip, but it is hardly possible for a pre-existing fault to slip comparatively to the rest of the models (Figs. 10 and 11). However, the orientation of the stress field is now critically affected and all models imply conditions of dike propagation.

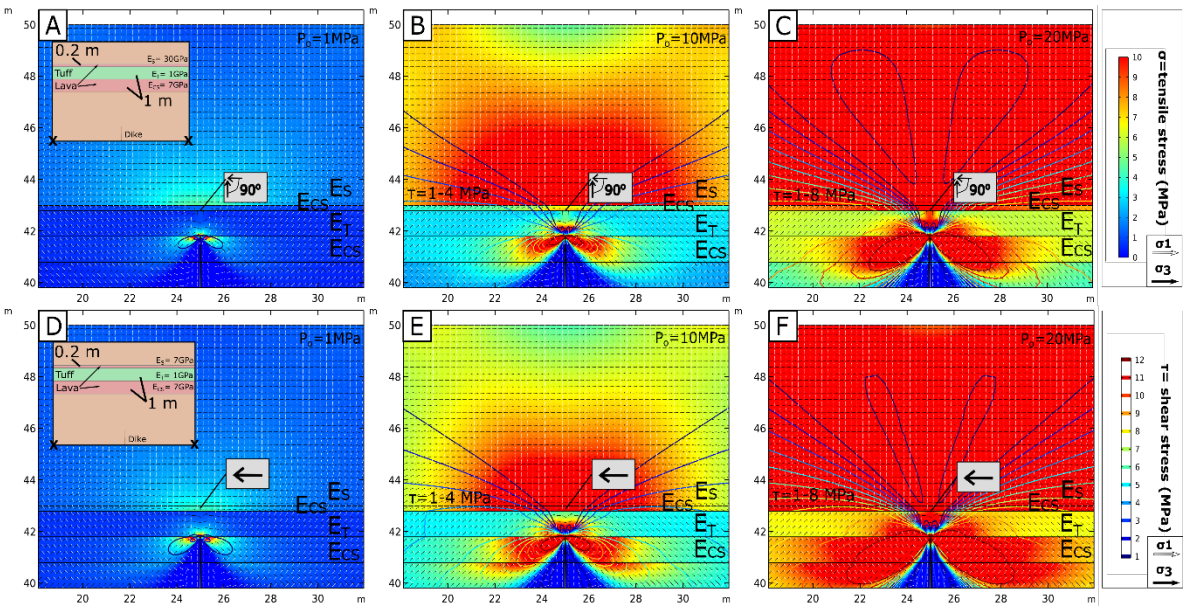

Figure 9. *FEM models show the distribution of tensile (σ) and shear stresses (τ) (contours) around a propagating dike tip. The models include the trajectories of the maximum principal compressive stress (σ_1, white arrows) and minimum principal compressive stress (σ_3, black arrows) in different concepts of layered media as denoted in the inset model maps. The colour scale of tensile and shear stresses ranges from 0-10 MPa and 0-12 MPa, respectively. (A, D) a vertical dike emplaced*

in the shallow crust with an overpressure of 1 MPa., (B, E) a vertical dike emplaced in the shallow crust with an overpressure of 10 MPa, (C, F) a vertical dike emplaced in the shallow crust with an overpressure of 20 MPa.

In the next stage, we altered the geometrical properties of the host rock (sequence of the stratigraphy and thickness of the layers) to identify discrepancies which could propose different surface deformation scenarios. Here, we present the model suites that have provided the most relevant insights (Figs. 10 and Fig. S2 Suppl.). In this model run, we have changed the thickness of the tuff layer by making it an order of magnitude thinner (W_T=0.1 m) (Figs. 10A-C) and decreased the heterogeneity of the host rock by omitting the tuff layer from the sequence (Figs. 10D-F). We have rerun the models with the same boundary loading conditions (P_o=1-20 MPa) and the same stiffness values (1-30 GPa). The results of the suites where P_o=1 MPa (Figs. 10D and Fig. S2 Suppl.) show similarities with Figs. 9A and Fig. S1 (Suppl.) implying 90° stress rotations and satisfied dike arrest conditions, while Fig. 10A shows rotations up to 80° only. However, if P_o=10 MPa (Figs. 10B and 10E) and the tuff layer is thinner by an order of magnitude (Fig. 10B), the shear stress distribution is again symmetrical to the dike tip, but appears to rise closer to the surface and to concentrate above it. The contours in the top lava layer range between 1-7 MPa while in the tuff layer they are between 2-6 MPa. Similarly, the theoretical shear stresses at the dike tip reach a maximum of 32 MPa and 9 MPa close to the surface that imply a higher probability of dike-induced faulting since the shear stress values are now 2.3 times higher (from 14 to 32 MPa) subject to the model results in Fig. 9. However, if the tuff layer lacks from the sequence (Fig. 10E), the distribution of shear stresses is again symmetrical but it is distributed higher and wider above the tip. The range of shear stress also differs from the previous runs with the amount to be 1-4 MPa in the lava layer and 1-5 MPa in the tuff layer (Fig. 10E) and the theoretical stresses to be two times higher than the results related to the models in Fig. 9 but lower than the results shown in Figs. 10A,D. In both models in Figs. 10B,E, the tensile stress distribution is sufficient (over 0.5 MPa) to make a fracture at the dike tip and it is concentrated similarly at the stiffer materials (lavas). In Figure 10B, the

trajectories of σ_1 and σ_3 arrow surfaces show no stress rotations at the vicinity of the tips but in Figure 10 E an 80° stress rotation is evident. Thus, in both case scenarios the dike cannot probably stall in the shallow crust.

In the next models (Figs. 10C and 10F), we increased the amount of overpressure (P_o=20 MPa) while keeping the same stiffness values (1-30 GPa). We observed no stress rotations at Fig. 10C and almost 90° rotations at Fig. 10F. The tensile stress concentration is also very high at the vicinity of the dike and closer to the surface. Especially in Figure 10F we observe a stronger bull's eye effect just above the dike tip, which could propose a wider distribution of Mode I fractures to the surface. Finally, the shear stress contours in Figure 10C have shown a very high distribution in the top lava layer (1-12 MPa) and just 1-7 MPa in the following run in Figure 10F, where the tuff layer is omitted. The theoretical shear stresses (Figs. S2A-L Suppl.) at the dike tip rise up to 64 MPa if the tuff layer is thin (Fig. 10C) and up to 54 MPa if the tuff layer is omitted from the stratigraphy. Close to the surface, the shear stresses can reach a maximum value of approximately 18 MPa when the thin tuff is present and 13.2 MPa when the tuff is absent. Those results could imply two possible volcanotectonic events. Mode I conditions suggest that a dike arrest scenario of a propagating dike could be likely. However, Mode II conditions, individually, can also imply that a dike-induced scenario is highly possible.

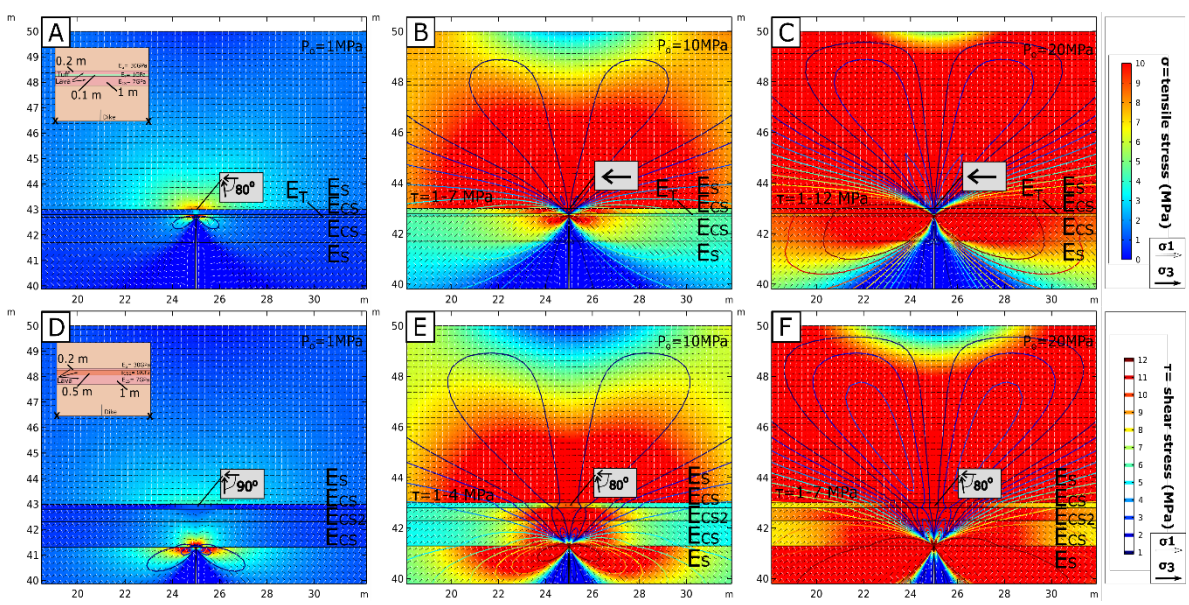

Figure 10. *FEM models show the distribution of tensile (σ), and shear stresses (τ) (contours) around a propagating dike tip. The models include the trajectories of the maximum principal compressive stress (σ_1, white arrows) and the minimum principal compressive stress (σ_3, black arrows) in different concepts of layered media as denoted in the inset model maps. The colour scale of tensile and shear stresses ranges from 0-10 MPa and 0-12 MPa, respectively. (A, D) A vertical dike emplaced in the shallow crust with an overpressure of 1 MPa, (B, E) A vertical dike emplaced in the shallow crust with an overpressure of 10 MPa, (C, F) a vertical dike emplaced in the shallow crust with an overpressure of 20 MPa*

In the last model runs, we repeated the exact same configuration similar to Figures 10A-F, assuming now an inclined dike (10° inclination) propagating towards the surface through a layered sequence. Now the concentration of tensile and shear stresses is asymmetrical and only the right part of the distribution (and shear stress lobe) reaches the surface. In the first model runs (P_o=1 MPa) (Fig. 11A,D) the tensile stress concentration patterns are consistent with the previous models (Figs. 9 and 10). The shear stresses are assymetrical at the tip with the right and left sides to reach theoretical values of 3.5 and 3.1 MPa, respectively, when the tuff layer is very thin (Figs. 11A and S3A Suppl.). In case the tuff layer is totally missing from the stratigraphy (Figs. 11D and S3G Suppl.) then the difference is even higher with 3.5 MPa for the right side and only 2.7 MPa for the left one. The trajectories of σ_1 and σ_3 arrow surfaces show stress rotations (0-45°) at the close vicinity of the tips but almost 90° rotations at the thin lava layers atop providing further insights in the conditions where stiff layers can be temporary stress barriers too.

Similarly, when the overpressure is P_o=10 MPa (Fig. 11B) the contours are concentrated at the top lava layer in a range between 1-8 MPa for the thin tuff layer scenario and between 1-4 MPa for the no tuff scenario. In both cases, they are distributed closer to the surface. The tensile stresses are high (8-10 MPa) and the theoritical shear stresses at the tips reach assymetrically a maximum of 34 MPa for both scenarios. Closer to the surface those values reach a maximum of 10.5 MPa at the right side of the models. The trajectories of σ_1 and σ_3 arrow surfaces show minor

stress rotations (0-45°) (Fig. 11B) and up to 80° on the comparatively stiff lava layer (Fig. 11E) so stress barriers are quite unlikely to form. In case the overpressure is higher (P_o=20 MPa) (Fig. 11C,F) the shear stress contours are denser in the lava layer with a range of 1-12 MPa. The tensile stresses are very high (9-10 MPa) at the top layer while the theoretical shear stress values peak in both stratigraphic scenarios at approximately 70 MPa at the dike tip and between 17-20 MPa close to the surface. The stress rotations are similar to Figs. 11B and 11E.The results could imply a successful shear fracturing mode at the right side and individually the formation of pure Mode I fractures at the left side of the dike tip.

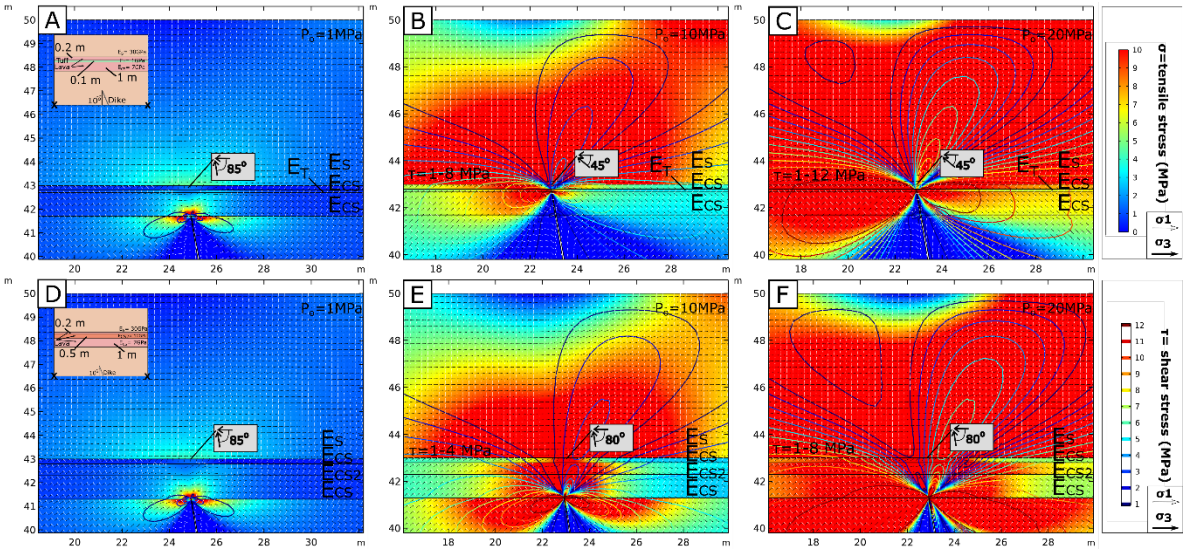

Figure 11. *FEM models show the distribution of tensile (σ), and shear stresses (τ) (contours) around a propagating dike tip. The models include the trajectories of the maximum principal compressive stress (σ_1, white arrows) and the minimum principal compressive stress (σ_3, black arrows) in different concepts of layered media as denoted in the inset model map. The Colour scale of tensile and shear stresses ranges from 0-10 MPa and 0-12 MPa, respectively. (A, D) An inclined dike (10°) emplaced in the shallow crust with an overpressure of 1MPa (B, E) An inclined dike (10°) emplaced in the shallow crust with an overpressure of 10 MPa, (C, F) an inclined dike (10°) emplaced in the shallow crust with an overpressure of 20 MPa.*

5. Discussion

The relation between surface deformation (width and displacement) and dike geometry is a crucial topic in volcanotectonics: several studies have been carried out both along slow and fast divergent plate boundaries, using field observations associated with geophysical data, such as GPS, InSAR, seismicity and analogue and numerical models (Tryggvason, 1984; Stein et al., 1991; Rubin, 1992; Chadwick and Embley, 1998; Wright et al., 2006; Calais et al., 2008; Ebinger et al., 2008; Pallister et al., 2010; Nobile et al., 2012; Sigmundsson et al., 2015; Agustdottir et al., 2016; Hjartardottir et al., 2016; Ruch et al., 2016; Xu et al., 2016; Al Shehri and Gudmundsson, 2018; Trippanera et al., 2019; Acocella 2021).

From a mechanical perspective, theoretical and analogue models by Pollard et al. (1983) and Mastin and Pollard (1988), with examples from Kilauea and the Inyo Craters, respectively, have provided major insights into the formation of dike-induced grabens in volcanic edifices. In detail, the experimental analyses of shallow dike intrusion processes have shown that new fractures are initially generating at the interior parts of pre-existing fractures and in the opposite sides of the dike plane very close to the surface. In layered domains, stiffer materials (e.g. lavas) tend to concentrate the extensional fractures and softer materials (e.g. tuffs) the shearing. Two scenarios of dike-induced surface deformation have been explored: i) Rise of overpressure at a static dike tip due to the presence of pore pressure (water and gas flow) and hydraulic fracturing pressure. The tip becomes locally compressed and more fracture growth occurs. Additionaly, subject to the material's resistance to compression, thrust faults can also be formed; ii) A dike propagates upward. The probability of extensional fracture growth at the surface is even higher. At the same time, the lower parts of pre-existing faults can become locked (Rubin and Pollard, 1988) and new normal faults can grow.

In both scenarios, during the inelastic deformation stage, the strain, instead of forming new extensional fractures, shifts on becoming accommodated in shear ones. The fractures can then coalesce and form graben structures. However, although these models consider a dike intruding in an elastic and homogeneous half-space medium, the influence of anelastic deformation, as well as the heterogeneity of the

crust are not considered. Similarly, the large width of a graben according to analogue models (Acocella and Trippanera, 2016) suggests that it could have been developed during dike ascent in depth. Field studies, though, document that dike-induced grabens can only occur in/close to the surface and they are highly associated with the combination of tectonic and dike-induced processes (Gudmundsson, 2020).

From a numerical perspective, dike-induced grabens are complex scenarios. Previous numerical studies (Al Shehri and Gudmundsson, 2019) showed that the majority of dikes are getting arrested due to layering of the shallow crust and that only in the very shallow parts of it graben formation will occur. For this scenario, a dike should be sufficient to mechanically break the host rock (tensile stress between 0.5-6 MPa) and propagate towards the surface. Then the shear stress (τ) concentration will be sufficient to cause pre-existing fractures to slip. The range of shear stress failure in brittle rocks is from 1-12 MPa, and usually two times the tensile stress ($\tau \geq 2\sigma$) making a reactivation scenario quite possible. In addition, the conditions under which Mode I and II fracturing occurs are diverse. Last but not least, the actual mechanism for fracture initiation imply mixed modes and not purely Mode I or II fracturing (Backers and Stephansson, 2012). Hence combining FEM modelling with other techniques such as dislocation modelling (e.g. Rivalta et al., 2002; Maccaferri et al., 2010) can give further and broader insights on faulting and fissuring from dike intrusion.

On Mt Etna especially, Murray and Pullen (1984) carried out a study about magma propagation during the 1983 eruption, using levelling data by modelling dike propagation in an elastic half-space. During the 2001 eruption, Acocella and Neri (2003) reported the formation of several grabens and fractures at the surface, and assumed the depth of the dike using the relation suggested by Pollard et al. (1983) and Mastin and Pollard (1988). Furthermore, the formation of an asymmetric graben was observed during both the 2008 and 2013 events; the depth of the dike was assumed from the width of the graben with the above-described relation, without further investigation (Bonaccorso et al., 2011; Falsaperla and Neri, 2015).

The structural analysis along with the numerical study of the 1928 fissure of Mt Etna presented here, provide insights into the distribution of surface deformation related

to dike-induced processes. Initially, our volcanotectonics study reports the type of deformation related to the formation of four different sectors as classified from field observations. In a second stage, our numerical models, in conjunction with the existing theoretical and experimental knowledge in dike intrusion processes, tries to answer the question related to how those deformation events occurred. In specific, in our stationary numerical model setups, we explored mainly the effects of: 1) layering above a propagating dike tip (E=1-30 GPa), and 2) different overpressure values of a basaltic dike (P_o=1-20 MPa). These conditions were specifically chosen since they reflect the heterogeneity of Etna's crustal segments and the shallow degassing processes that occur during Strombolian eruptions. In the following synthesis we provide a more detailed analysis of the distinct scenarios.

5.1 Volcanic vents and symmetric graben

Near the rim of the Valle del Bove, the 1928 fissure was characterized by important Strombolian activity with the emplacement of a series of volcanic vents with explosive crater-like morphopolgy and surrounded by small spatter and scoria ramparts (Sector 1). The vents are aligned ENE; each one is elongated in the same direction, and the ramparts are also elongated ENE, parallel to the trend of the 1928 fracture zone: these three features (Tibaldi, 1995; Tibaldi et al., 2013) clearly indicate that the pyroclastic emplacement was controlled by a dike striking ENE.

We suggest that in this segment, the dike produced the formation of a wide graben, as indicated by the presence of the two normal fault sets dipping inward and striking subparallel to the alignment of the vents. As is well known, the 1928 fracture propagated eastward (Branca et al., 2017); the vents' size decreases eastward, until they reach the fracture segment where only lavas and spatter were outpoured.

In our models, graben formation towards the surface occurs when two conditions are met: i) the shear stress concentration needs to become higher than the tensile stress ($\tau \geq 2\sigma$), and ii) the shear stress distribution, as shown by the contours surface and the theoretical shear stresses, needs to be expanded towards the surface. The previous conditions imply that dike-induced scenarios are more possible in layered domains with high stiffness contrasts (e.g. the existence of stiff, comparatively stiff

and soft materials) subject to high overpressure values (10-20 MPa) such as in the models of Figure 10. The latter could possibly imply the conditions of narrow or wide graben formation. As a consequence of the extra geometrical heterogeneity we modelled here, in case the soft layer is thin, the possible graben will be narrower than when the soft layer totally lacks from the stratigraphy. In the latter conditions, a wider graben can be formed. All those are subject to the mechanical state that a temporary stress barrier will not arrest the dike towards the surface, a condition that is, however, highly possible as shown in the models.

5.2 Single fracture vs. half-graben

East of Sector 1 is the area characterised by a single extension fracture with a length of 2 km. Here, there is also evidence of minor Strombolian activity, with ramparts of limited height. No graben developed along Sector 2. Further east is Sector 3, marked by the occurrence of the half-graben.

Actually, field data indicate the presence of both normal faults and extension fractures to the east, in line with the fact that natural rocks are neither purely Coulomb solids nor purely elastic, but instead behave like elasto-plastic materials (Jaeger et al., 2009; Gudmundsson, 2011): this means that both deformation mechanisms can occur during magma propagation and emplacement. Although in the past it has been proposed that inelastic deformation is negligible during magma propagation (e.g. Rubin, 1993), further field and geophysical data are demonstrating that shear failure is a fundamental process of magma propagation at the sheet tip (Gudmundsson et al., 2008; White et al., 2011; Ágústsdóttir et al., 2016; Spacapan et al., 2017). The segments of the 1928 structure represented by the single extension fracture and by the half-graben are located in a plain formed by a series of wide horizontal lava flows; thus, the host rocks around the dike have very similar characteristics in the two segments. Moreover, dike propagation occurred in a few days and thus variations in magma composition are not expected in a very short time and at close distance. Based on these observations, we cannot consider that the change from elastic deformation to fault shear is imputable to a change in the lithological characteristics of the host rock, as proposed for other areas by Vachon

and Hieronymus (2016), or to the intrusion of new magma with high viscosity (Spacapan et al., 2017).

Our numerical study provides further insights into the field observations. A scenario as seen in the field can be replicated by the numerical models shown in Figure 11. An inclined dike can produce assymetrical stresses which can result in different fracturing conditions around the dike and the formation of a half-graben; scenarios which can occur individually as possibilities. The change in plan view of the surface structures from a rectilinear geometry to the west, to a right-stepping geometry to the east, can be linked to an en-échelon arrangement of the dike. We suggest that the change in the style of deformation has occurred not only because of the dike inclination or the specific geometrical and mechanical conditions studied here but possibly also due to dike depth and tip shape variations. This hypothesis is based on the analogue models of Guldstrand et al. (2017), who proposed that the possible change in shape of the dike tip from a sharp one to a narrow one is in correspondence with a single extension fracture, while to a blunt or rectangular shape in correspondence with a half-graben. Finally, from a mechanical perspective, our numerical models propose that the formation of a single fracture possibly overlaps with the concept of a successful Mode I fracture scenario where a Mode II one is not satisfied. Conversely, a semi graben shall be formed when both scenarios are satisfied, but the shear stress is distributed asymmetrically above a propagating inclined tip.

5.3 1928 fracture and Ripe della Naca Faults

At the eastern termination of the 1928 fracture, the dike encountered the upper fault of the Ripe della Naca faults that worked as plane of weakness, steering the magma towards the surface. Dike deflection as such, through pre-existing fractures, is a challenging concept not only due to the mechanical complexity of the process but mostly due to the limited field examples where those processes can be observed in situ. Previous numerical analyses by Drymoni et al. (2021) provided insights into the encounter between vertical dikes and inclined faults at the Santorini caldera, Greece. The numerical study proposed that deflection occurs when the pre-existing pathway

is economical for the dike. Such a scenario is mainly associated with active heterogeneous or homogeneous fault cores, and steeply dipping dike-fault angles as well as low values of tensile strength (T_o) which can even be close to zero (Gudmundsson, 2020). Similarly, Browning and Gudmundsson (2015) have explored several scenarios subject to dissimilar intrusion properties and boundary conditions. In their models, caldera ring faults channelled and deflected inclined sheets forming circumferential ring dikes in the Hafnarfjall extinct volcano, west Iceland. Further, analytical and numerical studies of dike-fault capture related to high-angle faults at small depths in Nevada, USA, have been also reported (Gaffney et al., 2007). Finally, other studies have explored reactivated magma pathways at the Tamburiente caldera, Spain (Thiele et al., 2021), proposing that the dissimilar elastic properties of the magma-filled fractures combined with those of the host rock can arrest and divert dikes and form multiple dikes.

Numerically, in our case study, a chanelling scenario is satisfied if only Mode I conditions are prone to occur in the models but the Mode II fracturing type is not satisfied. This is explicitly showed in the models of Figure 9, where we observe that although the shear stresses are rising above the dike tip, they are not sufficient to generate high stresses which can consequently reactivate pre-existing fractures in the vicinity of the dike. This is mainly due to the existence of the thick tuff layer that suppresses the distribution of the stresses towards the surface.

5.4 Upwarping and regional considerations

In regard to topographic upwarping, we noticed that this process occurred at very local sites. Thus, the translation of the host rock in the direction of upward propagation of the dike was a very minor process. Our data are more in line with the model that predicts that the propagation of a dike occurs essentialy through the gradual lateral expansion of the dike sides (Trippanera et al., 2015).

At a more regional scale, we noticed that the right-stepping arrangement of the 1928 surface structures occurs at two zones: the first where the 1928 fracture zone passes from the bottom of the Valle del Bove to its upper rim, thus where the 1928 dike crosscuts a major, 130-m-high topographic scarp. The second zone of right-stepping

also occurs in correspondence of the crosscut with another topographic major feature, represented by the 90-130-m-high escarpment of the upper Ripe della Naca normal fault. We thus suggest that the dike was diverted southward, creating the right-stepping shallow structures, as a consequence of the gravitational unbuttressing due to the presence of these two topographic anomalies, whereas the dike maintained its straightness where the topography is characterized by an essentially constant low slope angle.

Again from a regional point of view, the general orientation of the 1928 fracture zone is sub-orthogonal to the dominant sliding direction of the eastern flank of Etna volcano, and is parallel to the Ripe della Naca faults. These observations support the idea that the emplacement of the 1928 dike was assisted by a favourable regional state of stress imputable to the process acting at this volcano flank. All available data, in fact, indicate that the eastern Etna flank is slowly sliding eastward under the effect of gravity forces and forceful intrusion of dikes (Borgia et al., 1992; Groppelli and Tibaldi, 1999; Tibaldi and Groppelli, 2002; Walter et al., 2005; Neri and Acocella, 2006; Neri et al., 2004, 2007, 2009; Solaro et al, 2010; Ruch et al., 2012; Siniscalchi et al., 2012; Azzaro et al., 2013; Bonforte et al., 2013; Le Corvec et al., 2014; Urlaub et al., 2018; De Novellis et al., 2019). Decompression due to flank sliding favours magma rising, which in turn further destabilizes the volcano flank and may induce acceleration in the flank slip (Acocella et al., 2003; Neri et al., 2004, 2009; Pezzo et al., 2020). The favourable orientation of the 1928 fracture is consistent also with the presence of other possible dike injections that occurred in the same area with the same orientation, such as: i) the fissure eruption of 1971, located about 2 km south of the 1928 structure, ii) the swarm of parallel fractures of pre-1928 age (green lines in Fig. 2), and iii) other ENE-trending series of Holocene pyroclastic cones in the conterminous area. Extensional deformations following a σ_3 trending about NW-SE also occurred in the past in the same location, as exemplified by the Ripe della Naca normal faults. The repeated dyke injection along this ENE Rift might also have been favoured by local focused extension induced by the development of a rollover structure, which originated in consequence of the volcano flank sliding above a listric detachment, as suggested by Ruch et al. (2010).

6. Conclusions

The study of the 1928 fissure eruption is of paramount importance not only for a better understanding of this event, that posed a high hazard and risk to the local population and infrastructures, but also for a general understanding of the processes that link dike emplacement and surface deformation. This is useful for a correct interpretation of deformation data monitoring that might occur in the future under similar settings elsewhere.

Our study puts forward that not only dike characteristics contribute to dictate surface deformation, but also topography and stratigraphy of the host rock are strongly influential. These variations are mirrored at the surface by changes in the style of deformation, which can occur at very short distance, in the order of a few hundred meters.

In regard to topography, the possible rectilinear prolongation of an eruptive fissure can be forecast only in the case of a flat topography or a constant low slope angle. If important topographic escarpments are present in the surroundings, a deviation from straightness can be expected.

As far as dike characteristics and host rock are concerned, our models have shown that the rise of tensile stress depends on the stiffness of the materials (here dissimilar layers) and the applied overpressure in the system. Similarly, the growth of shear stress above a dike tip is also related quantitatively to the overpressure of the dike. However, our study for the first time enables to gain insights into the distribution of the theoretical shear stresses from the vicinity of the tip towards the surface. These analyses in different geometrical and mechanical conditions have shown that soft materials (e.g. tuff in our case study) tend to suppress the distribution of the shear stresses above a dike but not the stiffness of the top layer. Also, high values of overpressure are able to concentrate a greater range of tensile and shear stresses at the top layers but only the combination of specific geometric and mechanical conditions can finally define the possible fracture or dike induced graben scenario.

Acknowledgments

We acknowledge Joel Ruch and an anonymous reviewer for their constructive comments on an early version of the manuscript. This work has been carried out under the framework of the Task Force 2021-TF2 “Deformation and magmatic processes from the lithosphere to the surface: integrated multidisciplinary approaches”, Chair A. Tibaldi, of the International Lithosphere Program. This study has benefited from funding provided by Dipartimento della Protezione Civile (DPC) within the convention “All. A INGV-DPC”. This paper does not necessarily represent DPC official opinion and policies. We acknowledge the “Parco dell’Etna” (https://parcoetna.it/) for permission to perform the survey.

References

Abdelmalak, M.M.,Mourgues, R., Galland, O., Bureau, D., 2012. Fracture mode analysis and related surface deformation during dyke intrusion: results from 2D experimental modelling. Earth Planet. Sci. Lett. 359–360, 93–105.

Acocella V. (2021) Volcano-tectonic processes, Advances in Volcanology, Springer Nature, Switzerland.

Acocella, V., Neri, M. (2003). What makes flank eruptions? The 2001 Etna eruption and its possible triggering mechanisms. Bulletin of Volcanology, 65(7), 517-529.

Acocella V, Neri M. (2009) Dike propagation in volcanic edifices: overview and possible developments, Special Issue: Gudmundsson – Volcanoes, Tectonophysics, 471, 67-77, doi: 10.1016/j.tecto.2008.10.002.

Acocella, V., and Trippanera, D. (2016). How diking affects the tectonomagmatic evolution of slow spreading plate boundaries: Overview and model. Geosphere, 12(3), 867-883.

Acocella V., Behncke B., Neri M., D’Amico S. (2003): Link between major flank slip and eruptions at Mt. Etna (Italy). Geophys. Res. Lett., 30(24), 2286, doi:10.1029/2003GL018642.

Acocella V., Neri M., Scarlato P. (2006a), Understanding shallow magma emplacement at volcanoes: Orthogonal feeder dikes during the 2002–2003 Stromboli (Italy) eruption. Geophys. Res. Lett., 33, L17310, doi:10.1029/2006GL026862.

Acocella V., Porreca M., Neri M., Mattei M. and Funiciello R. (2006b), Fissure eruptions at Mount Vesuvius (Italy): insights on the shallow propagation of dikes at volcanoes. Geology, v. 34; no. 8; p. 673–676; doi: 10.1130/G22552.1.

Acocella V., Neri M., Sulpizio R. (2009), Dike propagation within active central volcanic edifices: constraints from Somma-Vesuvius, Etna and analogue models. Bull. Volcanol., 71:219–223, DOI 10.1007/s00445-008-0258-2.

Ágústsdóttir, T., Woods, J., Greenfield, T., Green, R. G., White, R. S., Winder, T., Brandsdóttir B., Steinthórsson S., and Soosalu, H. (2016). Strike-slip faulting during the 2014 Bárðarbunga-Holuhraun dike intrusion, central Iceland. Geophysical Research Letters, 43, 1495–1503. https://doi.org/10.1002/2015GL067423

Ágústsdóttir, T., Woods, J., Greenfield, T., Green, R. G., White, R. S., Winder, T., ... & Soosalu, H. (2016). Strike-slip faulting during the 2014 Bárðarbunga-Holuhraun dike intrusion, central Iceland. Geophysical Research Letters, 43(4), 1495-1503.

Al Shehri, A., & Gudmundsson, A. (2018). Modelling of surface stresses and fracturing during dyke emplacement: Application to the 2009 episode at Harrat Lunayyir, Saudi Arabia. Journal of Volcanology and Geothermal Research, 356, 278-303.

Azzaro R., A. Bonforte, S. Branca, F. Guglielmino, 2013. Geometry and kinematics of the fault systems controlling the unstable flank of Etna volcano (Sicily). J. Volc. Geotherm. Res., 251, 5-15.

Azzaro, R., Branca, S., Gwinner, K., Coltelli, M., 2012. The volcano-tectonic map of Etna volcano, 1:100.000 scale: an integrated approach based on a morphotectonic analysis from high-resolution DEM constrained by geologic, active faulting and seismotectonic data. Ital. J. Geosci. 131 (1), 153–170

Babiker, M., & Gudmundsson, A. (2004). The effects of dykes and faults on groundwater flow in an arid land: the Red Sea Hills, Sudan. Journal of Hydrology, 297(1-4), 256-273.

Backers T., Stephansson O., 2012. ISRM Suggested Method for the Determination of Mode II Fracture Toughness. Rock Mech Rock Eng (2012) 45:1011–1022 DOI 10.1007/s00603-012-0271-9

Bahat, D., 1980. Hertzian fracture, a principal mechanism in the emplacement of the British Tertiary intrusive centres. Geol. Mag. 117, 463–470.

Bates, R., Jackson, J.A., 1987. Glossary of Geology. 3rd edition.McGraw-Hill Book Company (788 pp.).

Battaglia M., Di Bari M., Acocella V., Neri M. (2011), Dike emplacement and flank instability at Mount Etna: Constraints from a poro-elastic-model of flank collapse, J. Volcanol. Geotherm. Res., 199, 153-164, doi:10.1016/j.jvolgeores.2010.11.005.

Becerril, L., Galindo, I., Gudmundsson, A., & Morales, J. M. (2013). Depth of origin of magma in eruptions. Scientific reports, 3(1), 1-6.

Bell, F.G., 2000. Engineering Properties of Soils and Rocks, 4th ed., Blackwell Oxford, UK.

Billi, A., Acocella, V., Funiciello, R., Giordano, G., Lanzafame, G., Neri, M. (2003): Mechanisms for ground-surface fracturing and incipient slope failure associated to the July-August 2001 eruption of Mt. Etna, Italy: analysis of ephemeral field data. J. Volcanol. Geotherm. Res., 122, 3-4, 281-294.

Bonaccorso, A., Bonforte, A., Calvari, S., Del Negro, C., Di Grazia, G., Ganci, G., ... & Boschi, E. (2011). The initial phases of the 2008–2009 Mount Etna eruption: A multidisciplinary approach for hazard assessment. Journal of Geophysical Research: Solid Earth, 116(B3).

Bonafede, M., Olivieri, M., 1995. Displacement and gravity–anomaly produced by a shallow vertical dyke in a cohesionless medium. Geophys. J. Int. 123, 639–652.

Bonforte A., Gambino S. and Neri M. (2009), Intrusion of eccentric dikes: The case of the 2001 eruption and its role in the dynamics of Mt. Etna volcano, Special Issue: Volcanoes, Tectonophysics, 471, 78-86, doi:10.1016/j.tecto.2008.09.028.

Bonforte A., Guglielmino, G. Puglisi, 2013. Interaction between magma intrusion and flank dynamics at Mt. Etna in 2008, imaged by integrated dense GPS and DInSAR data. Geochem. Geophys. Geosyst., 14, 2818-2835.

Borgia, A., Ferrari, L., & Pasquarè, G. (1992). Importance of gravitational spreading in the tectonic and volcanic evolution of Mount Etna. Nature, 357(6375), 231-235.

Branca, S., Coltelli, M., Groppelli, G., Lentini, F., 2011. Geological Map Of Etna Volcano, 1: 50,000 Scale. Ital. J. Geosci. 130 (3):265–291. http://dx.doi.org/10.3301/IJG.2011.15.

Branca, S., De Beni, E., Chester, D., Duncan, A., & Lotteri, A. (2017). The 1928 eruption of Mount Etna (Italy): Reconstructing lava flow evolution and the destruction and recovery of the town of Mascali. Journal of Volcanology and Geothermal Research, 335, 54-70.

Broek, D. (1982). Elementary engineering fracture mechanics. Springer Science & Business Media.

Browning, J., & Gudmundsson, A. (2015). Caldera faults capture and deflect inclined sheets: An alternative mechanism of ring dike formation. Bulletin of Volcanology, 77(1), 4. https://doi.org/10.1007/s00445-014-0889-4

Calais, E., d'Oreye, N., Albaric, J., Deschamps, A., Delvaux, D., Déverchere, J., ... & Wauthier, C. (2008). Strain accommodation by slow slip and dyking in a youthful continental rift, East Africa. Nature, 456(7223), 783-787.

Chadwick Jr, W. W., & Embley, R. W. (1998). Graben formation associated with recent dike intrusions and volcanic eruptions on the mid-ocean ridge. Journal of Geophysical Research: Solid Earth, 103(B5), 9807-9825.

De Novellis, V., Atzori, S., De Luca, C., Manzo, M., Valerio, E., Bonano, M., Cardaci C., Castaldo R., Di Bucci D., Manunta M., Onorato G., Pepe S., Solaro G., Tizzani P., Zinno I., Neri M., Lanari R., Casu F. (2019). DInSAR analysis andanalytical modeling of Mount Etna displacements: The December 2018volcano-tectonic crisis. Geophysical Research Letters,46. https://doi.org/10.1029/2019GL082467.

Drymoni, K., Browning, J., & Gudmundsson, A. (2020). Dyke-arrest scenarios in extensional regimes: Insights from field observations and numerical models, Santorini, Greece. Journal of Volcanology and Geothermal Research, 396, 106854.

Drymoni, K., Browning, J., & Gudmundsson, A. (2021). Volcanotectonic interactions between inclined sheets, dykes, and faults at the Santorini Volcano, Greece. Journal of Volcanology and Geothermal Research, 107294.

Duncan, A. M., Dibben, C., Chester, D. K., & Guest, J. E. (1996). The 1928 eruption of Mount Etna Volcano, Sicily, and the destruction of the town of Mascali. Disasters, 20(1), 1-20.

Ebinger, C. J., Keir, D., Ayele, A., Calais, E., Wright, T. J., Belachew, M., Hammond, J.O.S., Campbell, E., & Buck, W. R. (2008). Capturing magma intrusion and faulting processes during continental rupture: seismicity of the Dabbahu (Afar) rift. Geophysical Journal International, 174(3), 1138-1152.

Falsaperla S., Neri M. (2015), Seismic footprints of shallow dyke propagation at Etna, Italy. Sci. Rep. 5, 11908; doi:10.1038/srep11908.

Farmer, I., 1983. Engineering Behaviour of Rocks, 2nd ed.; Chapman and Hall: London, UK.

Ferrari, L., Garduño, V.H., Neri, M. (1991). I dicchi della Valle del Bove, Etna: un metodo per stimare le dilatazioni di un apparato vulcanico. Mem. Soc. Geol. It, 47, 495-508, 9 figg., 2 tabb.

Fittipaldi M., Urbani S., Neri M., Trippanera D., Acocella V. (2019), Understanding the origin of magmatic necks: insights from Etna and analogue models, Bull Volcanol., 81:11, https://doi.org/10.1007/s00445-019-1273-1.

Friedlander, I., 1929. Vulkanische ereignisse. Der Atna-Ausbruch 1928. Zeitschrift fur Vulkanologie, Band XII. pp. 33–46.

Gaffney, E. S., Damjanac, B., & Valentine, G. A. (2007). Localization of volcanic activity: 2. Effects of pre-existing structure. Earth and Planetary Science Letters, 263(3), 323–338. https://doi.org/10.1016/j.epsl.2007.09.002

Galland, O., Holohan, E., de Vries, B. V. W., & Burchardt, S. (2015). Laboratory modelling of volcano plumbing systems: a review. Physical Geology of Shallow Magmatic Systems, 147-214.

Garagash, D., Detournay, E., 2000. The tip region of a fluid-driven fracture in an elasticmedium. ASME J. Appl. Mech., 67, 183–192.

Garduño, V.H., M. Neri, G. Pasquarè, A. Borgia and A. Tibaldi (1997): Geology of NE.Rift of Mount Etna, Sicily (Italy). Acta Vulcanol., Vol. 9 (1/2), 91-100.

Gautneb, H., Gudmundsson, A., Oskarsson, N., 1989. Structure, petrochemistry and evolution of a sheet swarm in an Icelandic central volcano. Geol. Mag. 126, 659–673.

Geshi N. and Neri M. (2014), Dynamic feeder dyke systems in basaltic volcanoes: the exceptional example of the 1809 Etna eruption (Italy). Front. Earth Sci. 2:13. doi: 10.3389/feart.2014.00013.

Groppelli, G., & Tibaldi, A. (1999). Control of rock rheology on deformation style and slip-rate along the active Pernicana Fault, Mt. Etna, Italy. Tectonophysics, 305(4), 521-537.

Gudmundsson, A. (2020). Volcanotectonics: Understanding the structure, deformation and dynamics of volcanoes. Cambridge University Press.

Gudmundsson, A. (2011). Rock fractures in geological processes. Cambridge University Press.

Gudmundsson, A., Brenner, S.L., 2001. How hydrofractures become arrested. Terra Nova, 13, 456–462.

Gudmundsson, A., Berg, S.S., Lyslo, K.B., Skurtveit, E., 2001. Fracture networks and fluid transport in active fault zones. J. Struct. Geol. 23, 343–353.

Gudmundsson, A., Friese, N., Galindo, I., Philipp, S.L., 2008. Dike-induced reverse faulting in a graben. Geology 36, 123–126. http://dx.doi.org/10.1130/G24185A.1.

Guldstrand, F., Burchardt, S., Hallot, E., & Galland, O. (2017). Dynamics of surface deformation induced by dikes and cone sheets in a cohesive Coulomb brittle crust. Journal of Geophysical Research: Solid Earth, 122(10), 8511-8524.

Gwinner, K., Coltelli, M., Flohrer, J., Jaumann, R., Matz, K.D., Marsella, M., Roatsch, T., Scholten, F., Trauthan, F., 2006. The HRSC-AX Mt. Etna project: high-resolution orthoimages and 1 m DEM at regional scale. ISPRS Com. I Symposium, Paris, France, 3–6 July 2006.

Haimson, B.C.; Rummel, F., 1982. Hydrofracturing stress measurements in the Iceland research drilling project drill hole at Reydarfjördur, Iceland. J. Geophys. Res., 87, 6631–6649

Heap, M. J., Villeneuve, M., Albino, F., Farquharson, J. I., Brothelande, E., Amelung, F., Got, J. L., & Baud, P. (2020). Towards more realistic values of elastic moduli for volcano modelling. Journal of volcanology and geothermal research, 390, 106684.

Hjartardóttir, Á. R., Einarsson, P., Gudmundsson, M. T., & Högnadóttir, T. (2016). Fracture movements and graben subsidence during the 2014 Bárðarbunga dike intrusion in Iceland. Journal of Volcanology and Geothermal Research, 310, 242-252.

Imbò, G., 1932. Osservazioni e ricerche in relazione all'eruzione etnea 2–20 Novembre 1928. Annali R. Oss. Vesuviano Vol. I pp. 293–349.

Jaeger, J. C., Cook, N. G., & Zimmerman, R. (2009). Fundamentals of Rock Mechanics. Malden, MA: John Wiley & Sons.Gudmundsson, 2011).

Lawn BR (1993) Fracture of Brittle Solids. Cambridge University Press, Cambridge

Le Corvec N., T.R. Walter, J. Ruch, A. Bonforte, G. Puglisi, 2014. Experimental study of the interplay between magmatic rift intrusion and flank instability with application to the 2001 Mount Etna eruption. J. Geophys. Res., 119, 5356-5368, 10.10022/2014JB011224

Maccaferri, F., Bonafede, M., & Rivalta, E. (2010). A numerical model of dyke propagation in layered elastic media. Geophysical Journal International, 180(3), 1107-1123.

Maccaferri, F., Bonafede, M., & Rivalta, E. (2011). A quantitative study of the mechanisms governing dike propagation, dike arrest and sill formation. Journal of Volcanology and Geothermal Research, 208(1-2), 39-50.

Melin S (1986) When does a crack grow under mode II conditions? Int J Fract 30:103–114

Mastin, L.G., Pollard, D.D., 1988. Surface deformation and shallowdike intrusion processes at Inyo Craters, Long Valley, California. J. Geophys. Res. 13221–13235.

Murray, J. B., & Pullen, A. D. (1984). Three-dimensional model of the feeder conduit of the 1983 eruption of Mt. Etna volcano, from ground deformation measurements. Bulletin Volcanologique, 47(4), 1145-1163.

Neri, M., Acocella, V., & Behncke, B. (2004). The role of the Pernicana Fault System in the spreading of Mt. Etna (Italy) during the 2002–2003 eruption. Bulletin of Volcanology, 66(5), 417-430.

Neri M., Acocella V., (2006), The 2004-05 Etna eruption: implications for flank deformation and structural behaviour of the volcano. J. Volcanol. Geotherm. Res., 158, 195-206, DOI:10.1016/j.jvolgeores.2006.04.022.

Neri M., Acocella V., Behncke B., Giammanco S., Mazzarini F., Rust D. (2011). Structural analysis of the eruptive fissures at Mount Etna (Italy). Ann. Geophys., 54, 5, 464-479, doi: 10.4401/ag-5332.

Neri M., F. Casu, V. Acocella, G. Solaro, S. Pepe, P. Berardino, E. Sansosti, T. Caltabiano, P. Lundgren, R. Lanari (2009), Deformation and eruptions at Mt. Etna (Italy): a lesson from 15 years of observations. Geophys. Res. Lett., 36, L02309, doi:10.1029/2008GL036151.

Neri M., Guglielmino F., Rust D. (2007), Flank instability on Mount Etna: radon, radar interferometry, and geodetic data from the southern boundary of the unstable sector. J. Geophys. Res., 112, B04410, doi:10.1029/2006JB004756.

Neri M., Lanzafame G., Acocella V., (2008). Dike emplacement and related hazard in volcanoes with sector collapse: the 2007 Stromboli eruption, J. Geol. Soc. London, 165, 883-886, doi:10.1144/0016-76492008-002.

Nobile, A., Pagli, C., Keir, D., Wright, T. J., Ayele, A., Ruch, J., & Acocella, V. (2012). Dike-fault interaction during the 2004 Dallol intrusion at the northern edge of the Erta Ale Ridge (Afar, Ethiopia). Geophysical Research Letters, 39(19).

Pallister, J. S., McCausland, W. A., Jónsson, S., Lu, Z., Zahran, H. M., El Hadidy, S., Aburukbah A., Stewart I.C.F., Lundgren P.R., White R.A. & Moufti, M. R. (2010). Broad accommodation of rift-related extension recorded by dyke intrusion in Saudi Arabia. Nature Geoscience, 3(10), 705-712.

Patanè D, Aliotta M., Cannata A., Cassisi C., Coltelli M., Di Grazia, G., Montalto P. and. Zuccarello L (2011). Interplay between Tectonics and Mount Etna's Volcanism: Insights into the Geometry of the Plumbing System, New Frontiers in Tectonic Research - At the Midst of Plate Convergence, Uri Schattner, IntechOpen, DOI: 10.5772/23503. Available from: https://www.intechopen.com/chapters/17661

Pezzo, G., Palano, M., Tolomei, C., De Gori, P., Calcaterra, S., Gambino, P., & Chiarabba, C. (2020). Flank sliding: A valve and a sentinel for paroxysmal eruptions and magma ascent at Mount Etna, Italy. Geology, 48(11), 1077-1082.

Pollard, D. D., & Johnson, A. M. (1973). Mechanics of growth of some laccolithic intrusions in the Henry Mountains, Utah, II: bending and failure of overburden layers and sill formation. Tectonophysics, 18(3-4), 311-354.

Pollard, D.D., Delaney, P.T., Duffield, W.A., Endo, E.T., Okamura, A.T., 1983. Surface deformation in volcanic rift zones. Tectonophysics 94, 541–584.

Ponte, G., 1928. L'eruzione etnea del novembre 1928. Rivista di Fisica, Matematica e Scienze Naturali, Vol. III, 113–122, Napoli.

Ponte, G., 1929. Bollettino dell'Istituto Vulcanologico Etneo. Rivista dell'-Industria, Anno II (12), December 1928. Tip. C., Galàtola, Catania.

Ray, R., Sheth, H. C., Mallik, J. (2007). Structure and emplacement of the Nandurbar–Dhule mafic dyke swarm, Deccan Traps, and the tectonomagmatic evolution of flood basalts. Bulletin of Volcanology, 69(5), 537-551.

Rivalta, E., Mangiavillano, W., Bonafede, M. (2002). The edge dislocation problem in a layered elastic medium. Geophysical Journal International, 149(2), 508-523.Rubin, A.M., Pollard, D.D., 1988. Dike-induced faulting in rift zones of Iceland and Afar. Geology 16 (5), 413–417.

Rubin, A. M. (1993). Tensile fracture of rock at high confining pressure: Implications for dike propagation. Journal of Geophysical Research, 98(B9), 15,919–15,935.

Rubin, A. M. (1992). Dike-induced faulting and graben subsidence in volcanic rift zones. Journal of Geophysical Research: Solid Earth, 97(B2), 1839-1858.

Ruch, J., Acocella, V., Storti, F., Neri, M., Pepe, S., Solaro, G., & Sansosti, E. (2010). Detachment depth revealed by rollover deformation: An integrated approach at Mount Etna. Geophysical Research Letters, 37(16).

Ruch J., Pepe S., Casu F., Acocella V., Neri M., Solaro G., Sansosti E. (2012), How do rift zones relate to volcano flank instability? Evidence from collapsing rifts at Etna, Geophys. Res. Lett., 39, L20311, doi:10.1029/2012GL053683.

Ruch, J., Wang, T., Xu, W., Hensch, M., & Jónsson, S. (2016). Oblique rift opening revealed by reoccurring magma injection in central Iceland. Nature communications, 7(1), 1-7.

Schultz, R.A., 1995. Limits on strength and deformation properties of jointed basaltic rock masses. Rock Mech. Rock Eng., 28, 1–15.

Sigmundsson, F., Hooper, A., Hreinsdóttir, S., Vogfjörd, K. S., Ófeigsson, B. G., Heimisson, E. R., & Eibl, E. P. (2015). Segmented lateral dyke growth in a rifting event at Bárðarbunga volcanic system, Iceland. Nature, 517(7533), 191-195.

Sili, G., Urbani, S., & Acocella, V. (2019). What controls sill formation: An overview from analogue models. Journal of Geophysical Research: Solid Earth, 124(8), 8205-8222.

Solaro G., Acocella V., Pepe S., Ruch J., Neri M., Sansosti E., (2010), Anatomy of an unstable volcano through InSAR data: multiple processes affecting flank instability at Mt. Etna in 1994-2008. J. Geophys.Res., 115, B10405, doi:10.1029/2009JB000820.

Spacapan, J. B., Galland, O., Leanza, H. A., & Planke, S. (2017). Igneous sill and finger emplacement mechanism in shale-dominated formations: A field study at Cuesta del Chihuido, Neuquén Basin, Argentina. Journal of the Geological Society, 174(3), 422–433. https://doi.org/10.1144/jgs2016-056

Stein, R. S., Briole, P., Ruegg, J. C., Tapponnier, P., & Gasse, F. (1991). Contemporary, Holocene, and Quaternary deformation of the Asal Rift, Djibouti: Implications for the mechanics of slow spreading ridges. Journal of Geophysical Research: Solid Earth, 96(B13), 21789-21806.

Thiele, S. T., Cruden, A. R., Zhang, X., Micklethwaite, S., & Matchan, E. L. (2021). Reactivation of magma pathways: Insights from field observations, geochronology, geomechanical tests, and numerical models. Journal of Geophysical Research: Solid Earth, 126(5), e2020JB021477.

Tibaldi, A., 1995. Morphology of pyroclastic cones and tectonics. Journal of Geophysical Research: Solid Earth, 100(B12), 24521-24535.

Tibaldi, A., 2015. Structure of volcano plumbing systems: a review of multi-parametric effects. J. Volcanol. Geotherm. Res., 298, 85–135.

Tibaldi, A., & Groppelli, G., 2002. Volcano-tectonic activity along structures of the unstable NE flank of Mt. Etna (Italy) and their possible origin. Journal of Volcanology and Geothermal Research, 115(3-4), 277-302.

Tibaldi, A., Vezzoli, L., Pasquarè, F.A.,Rust, D., 2008. Strike-slip fault tectonics and the emplacement of sheet–laccolith systems: the Thverfell case study (SW Iceland). J. Struct. Geol. 30, 274–290.

Tibaldi, A., Bonali, F. L., Pasquaré, F. A., Rust, D., Cavallo, A., & D'urso, A. (2013). Structure of regional dykes and local cone sheets in the Midhyrna-Lysuskard area, Snaefellsnes Peninsula (NW Iceland). Bulletin of volcanology, 75(11), 1-16.

Tibaldi, A., Bonali, F. L., Russo, E., & Fallati, L. (2020). Surface deformation and strike-slip faulting controlled by dyking and host rock lithology: A compendium from the Krafla Rift, Iceland. Journal of Volcanology and Geothermal Research, 395, 106835.

Trippanera, D., Acocella, V., & Ruch, J. (2014). Dike-induced contraction along oceanic and continental divergent plate boundaries. Geophysical Research Letters, 41(20), 7098-7104.

Trippanera, D., Ruch, J., Acocella, V., & Rivalta, E. (2015). Experiments of dike-induced deformation: insights on the long-term evolution of divergent plate boundaries. Journal of Geophysical Research: Solid Earth, 120(10), 6913-6942.

Trippanera, D., Ruch, J., Passone, L., & Jónsson, S. (2019). Structural mapping of dike-induced faulting in Harrat Lunayyir (Saudi Arabia) by using high resolution drone imagery. Frontiers in Earth Science, 7, 168.

Tryggvason, E. (1984). Widening of the Krafla fissure swarm during the 1975–1981 volcano-tectonic episode. Bulletin volcanologique, 47(1), 47-69.

Urlaub M., F. Petersen, F. Gross, A. Bonforte, G. Puglisi, F. Guglielmino, S. Krastel, D. Lange, H. Kopp, 2018. Gravitational collapse of Mount Etna Southeastern flank. Sci. Adv., 4, 10.1126/sciadv.aat9700

Vachon, R., & Hieronymus, C. F. (2016). Effect of host-rock rheology on dyke shape, thickness, and magma overpressure. Geophysical Journal International, ggw448, 1414–1429.

Walter, T.R., Acocella, V., Neri, M., Amelung, F., (2005), Feedback processes between magmatism and E-flank movement at Mt. Etna (Italy) during the 2002-2003 eruption. J. Geophys. Res., 110, B10205, doi:10.1029/2005JB003688.

Warpinski, H.R., 1985. Measurement of width and pressure in a propagating hydraulic fracture. J. Soc. Petrol. Eng. 46–54.

White, R. S., Drew, J., Martens, H. R., Key, J., Soosalu, H., & Jakobsdóttir, S. S. (2011). Dynamics of dyke intrusion in the mid-crust of Iceland. Earth and Planetary Science Letters, 304(3), 300–312.

Wright, T. J., Ebinger, C., Biggs, J., Ayele, A., Yirgu, G., Keir, D., & Stork, A. (2006). Magma-maintained rift segmentation at continental rupture in the 2005 Afar dyking episode. Nature, 442(7100), 291-294.

Xu, W., Jónsson, S., Corbi, F., & Rivalta, E. (2016). Graben formation and dike arrest during the 2009 Harrat Lunayyir dike intrusion in Saudi Arabia: Insights from InSAR, stress calculations and analog experiments. Journal of Geophysical Research: Solid Earth, 121(4), 2837-2851.